ORIGINAL ARTICLE

Journal of Cachexia, Sarcopenia and Muscle 2021; **12**: 933–954
Published online 13 June 2021 in Wiley Online Library (wileyonlinelibrary.com) **DOI:** 10.1002/jcsm.12742

Superiority of focused ion beam-scanning electron microscope tomography of cardiomyocytes over standard 2D analyses highlighted by unmasking mitochondrial heterogeneity

Jacqueline Heinen-Weiler[1,2†], Mike Hasenberg[2†], Martin Heisler[1], Stephan Settelmeier[1], Anna-Lena Beerlage[1], Hannah Doepper[1], Bernd Walkenfort[2], Andrea Odersky[1], Peter Luedike[1], Elke Winterhager[1,2], Tienush Rassaf[1] & Ulrike B. Hendgen-Cotta[1*]

[1]*Department of Cardiology and Vascular Medicine, West German Heart and Vascular Center, Medical Faculty, University of Duisburg-Essen, Essen, Germany*
[2]*Imaging Center Essen (IMCES), Electron Microscopy Unit (EMU), Medical Faculty, University of Duisburg-Essen, Essen, Germany*

Abstract

Background Cardioprotection by preventing or repairing mitochondrial damage is an unmet therapeutic need. To understand the role of cardiomyocyte mitochondria in physiopathology, the reliable characterization of the mitochondrial morphology and compartment is pivotal. Previous studies mostly relied on two-dimensional (2D) routine transmission electron microscopy (TEM), thereby neglecting the real three-dimensional (3D) mitochondrial organization. This study aimed to determine whether classical 2D TEM analysis of the cardiomyocyte ultrastructure is sufficient to comprehensively describe the mitochondrial compartment and to reflect mitochondrial number, size, dispersion, distribution, and morphology.

Methods Spatial distribution of the complex mitochondrial network and morphology, number, and size heterogeneity of cardiac mitochondria in isolated adult mouse cardiomyocytes and adult wild-type left ventricular tissues (C57BL/6) were assessed using a comparative 3D imaging system based on focused ion beam-scanning electron microscopy (FIB-SEM) nanotomography. For comparison of 2D vs. 3D data sets, analytical strategies and mathematical comparative approaches were performed. To confirm the value of 3D data for mitochondrial changes, we compared the obtained values for number, coverage area, size heterogeneity, and complexity of wild-type cardiomyocyte mitochondria with data sets from mice lacking the cytosolic and mitochondrial protein BNIP3 (BCL-2/adenovirus E1B 19-kDa interacting protein 3; $Bnip3^{-/-}$) using FIB-SEM. Mitochondrial respiration was assessed on isolated mitochondria using the Seahorse XF analyser. A cardiac biopsy was obtained from a male patient (48 years) suffering from myocarditis.

Results The FIB-SEM nanotomographic analysis revealed that no linear relationship exists for mitochondrial number ($r = 0.02$; $P = 0.9511$), dispersion ($r = -0.03$; $P = 0.9188$), and shape (roundness: $r = 0.15$, $P = 0.6397$; elongation: $r = -0.09$, $P = 0.7804$) between 3D and 2D results. Cumulative frequency distribution analysis showed a diverse abundance of mitochondria with different sizes in 3D and 2D. Qualitatively, 2D data could not reflect mitochondrial distribution and dynamics existing in 3D tissue. 3D analyses enabled the discovery that BNIP3 deletion resulted in more smaller, less complex cardiomyocyte mitochondria (number: $P < 0.01$; heterogeneity: C.V. wild-type 89% vs. $Bnip3^{-/-}$ 68%; complexity: $P < 0.001$) forming large myofibril-distorting clusters, as seen in human myocarditis with disturbed mitochondrial dynamics. $Bnip3^{-/-}$ mice also show a higher respiration rate ($P < 0.01$).

Conclusions Here, we demonstrate the need of 3D analyses for the characterization of mitochondrial features in cardiac tissue samples. Hence, we observed that BNIP3 deletion physiologically acts as a molecular brake on

mitochondrial number, suggesting a role in mitochondrial fusion/fission processes and thereby regulating the homeostasis of cardiac bioenergetics.

Keywords Cardiac mitochondria; Focused ion beam-scanning electron microscopy; BNIP3; 3D morphometry; Mitochondrial energetics; Mitochondrial dynamics

Received: 18 September 2020; Revised: 16 April 2021; Accepted: 21 May 2021
**Correspondence to: Ulrike B. Hendgen-Cotta, Department of Cardiology and Vascular Medicine, West German Heart and Vascular Center, Medical Faculty, University of Duisburg-Essen, Hufelandstraße 55, 45147 Essen, Germany. Phone: +49-201-723-6053, Fax: +49-201-723-6973, Email: ulrike.hendgen-cotta@uk-essen.de*
†Jacqueline Heinen-Weiler and Mike Hasenberg contributed equally to this study.

Introduction

Proper cardiac function is dependent on the complex orchestration of a variety of cellular and organelle components. Mitochondria comprise up to one-third of the cellular volume of a left ventricular (LV) cardiomyocyte.[1–3] The primary function of mitochondria is energy production, an important task, especially for cells with a high energy demand, such as cardiomyocytes, which show a high mitochondrial content. In line with their role in bioenergetic and biosynthetic pathways and serving as an important node for cellular Ca^{2+} signalling, they are also involved in cell growth, ion homeostasis, redox signalling, and cell survival.[1,3,4] Structural and functional integrity are maintained by the mitochondrial dynamism/turnover/mitophagy interactome under natural conditions.[5] Preclinical studies of mitochondrial dynamism have shown that the combined abrogation of fusion and fission provoked massive progressive mitochondrial accumulation in cardiomyocytes, severely distorting the sarcomere architecture.[6] Numerous studies have linked dysfunctional mitochondria and alterations in mitochondrial morphology to cardiac pathologies, including myocardial infarction and heart failure, with a focus on parameters of LV mitochondrial morphology, including shape, volume, size, number, and cristae density, even finding gender-specific differences.[7–12] Remarkably, studies have shown a connection between mitochondrial dysfunctions in skeletal and heart muscle. For example, myopathies like Duchenne muscular dystrophy are associated with mitochondrial dysregulations,[13] in which not only skeletal muscles are impaired[14] but also cardiac muscle cells are being damaged.[15] These cardiomyopathies also seem to arise from mitochondrial dysregulations.[16] To clearly characterize these morphological abnormalities among mitochondria, precise and reproducible image acquisition and analysis at the nanoscale is indispensable. Several publications have demonstrated a relationship between mitochondrial morphology and proper mitochondrial function,[10,17,18] but most of these studies relied on just two-dimensional (2D) routine transmission electron microscopy (TEM). Compared with conventional scanning electron microscopy (SEM), the Riva group has developed a high-resolution SEM with a high value for uncovering the membranous structure of heart mitochondria.[19–21] However, the detection of mitochondria in the real three-dimensional (3D) tissue in respect to localization, number, and shape variations is limited. To overcome the 2D limitations, different 3D EM analysis techniques, such as TEM tomography, serial block-face SEM (SBF-SEM), and focused ion beam-SEM (FIB-SEM) have been developed. FIB-SEM nanotomography is based on the integration of a high-energy ion beam into the column of an SEM system. FIB-SEM technique generates an image stack often consisting of several hundreds of single-image planes, which can subsequently be reconstructed *in silico* into a 3D model offering a wide variety of parameter analyses.[22]

In this study, we initially used FIB-SEM to accurately assess the spatial distribution of the complex mitochondrial network and the morphology of mouse cardiomyocyte mitochondria in isolated adult cardiomyocytes as well as in cardiac biopsies. We developed analytical strategies and defined comparative approaches to relate 2D data to results from 3D analyses. Thus, we elucidated deviations between analyses performed on either 2D or 3D data sets, which are important to properly describe and understand pathological conditions of cardiomyocyte mitochondria. To test the value of our 3D wild-type (WT) mouse analysis approach, we compared those data sets with 3D mitochondrial data sets generated from cardiac biopsies of *Bnip3*-deficient ($Bnip3^{-/-}$) mice. BNIP3 belongs to the BCL-2 family and regulates cell death *via* apoptosis as well as necrosis and mitophagy under pathological conditions.[23–25] It is associated with pathological LV remodeling[26] and the development of cardiac hypertrophy by mediating mitophagy, the inflammatory response and other related signalling pathways in cardiomyocytes.[27–29] The physiological role of cardiac BNIP3 remains unresolved. Hence, we used the FIB-SEM analysis approach to precisely characterize the cardiomyocyte mitochondrial compartment of $Bnip3^{-/-}$ mice compared with that of WT mice in a 3D manner.

Methods

Mice

All animal procedures were performed in accordance with institutional guidelines and approval from the local ethics committee in compliance with the European Convention for the Protection of Vertebrate Animals Used for Experimental and

other Scientific Purposes (Directive 2010/63/EU, 84-02.04.2014A144; 81-02.04.2019A369). Male WT mice (C57Bl/6J), aged 12 ± 5 weeks, were purchased from the Jackson Laboratory (Bar Harbour, ME, USA) and first acclimated at the local animal facility for one week. C57BL/6J-TgH (*Bnip3*$^{-/-}$ mice), aged 12 ± 5 weeks, were bred and nursed in the animal facility of the University Hospital Essen. All mice were kept under a 12 h light and dark cycle with unlimited access to water and food. For subsequent analyses, mice were killed by cervical dislocation.

Human patient

This study was approved by the University Hospital Essen Ethics Committee (17-7392-BO). The experiment was carried out in accordance with the approved guidelines. A cardiac biopsy was obtained from a male patient (48 years) suffering from myocarditis.

Isolation of adult mouse cardiomyocytes

Cardiomyocytes were isolated from the cardiac tissue of adult WT and *Bnip3*$^{-/-}$ mice. Immediately after cervical dislocation, the explanted heart was rapidly perfused through the aorta with a digestion solution containing 25 mM HEPES, 110 mM NaCl, 1.2 mM KH_2PO_4, 2.5 mM KCl, 2.5 mM $MgSO_4$, 100 μM $CaCl_2$, 10 mM glucose-monohydrate and 4 μM collagenase type II (pH 7.4). After 25 min of perfusion at 37°C, the cardiac tissue was fully disintegrated using a microtome (McIlwain Tissue Chopper, Mickle Laboratory Engineering Co., Ltd., Guildford, UK), and the resulting tissue was filtered through a 200 μm nylon mesh immediately before centrifugation at 100 × *g* for 1 min. The cell pellet was resuspended in 100 μM HEPES buffer, followed by four more centrifugation steps at 100 × *g*. Between each step, the supernatant was removed, and the pellet was resuspended in 100 μM HEPES buffer containing an incrementally increasing concentration of 100 mM $CaCl_2$ (0.125%, 0.25%, 0.5%, 1%). Ultimately, 24 × 10^3 cells were cultured in poly-L-lysine-coated cell culture dishes with a gridded glass bottom (MatTek Corporation, Ashland, USA) in modified Media 199 (100 IU/mL penicillin + 100 μg/mL streptomycin, 2 mM carnitine, 5 mM creatine, 5 mM taurine and 10 μM cytosine-D-arabinofuranoside) for 2.5 h at 37°C and 5% CO_2.

Staining and fluorescence imaging of isolated cardiomyocytes

Isolated cardiomyocytes from WT and *Bnip3*$^{-/-}$ were cultured in a laminin (Roche Diagnostics GmbH, Rotkreuz, Switzerland) coated 16 well chamber slide (Thermo Fisher Scientific, Waltham, Massachusetts, USA). Ultimately, 5 × 10^3 cells were seeded in each well. After 2 h, cells were stained with MitoTracker™ Orange (Thermo Fisher Scientific) for 15 min at 37°C, followed by fixation with 4% formaldehyde for 20 min at 37°C. Then the cells were permeabilized with phosphate buffered saline containing 0.5% Triton X-100 (Sigma Aldrich, St. Louis, Missouri, USA) for 5 min at room temperature (RT). Subsequently, non-specific binding sites were blocked with normal goat serum (Thermo Fisher Scientific) for 15 min at RT. After that, cells were stained with Alexa Fluor™ 488 Phalloidin (1 h at RT, Thermo Fisher Scientific) and 4′, 6-diamidino-2-phenylindole (DAPI) (15 min, RT, Thermo Fisher Scientific). Finally, gaskets were removed, and cells were embedded using ProLong™ Gold anti-fade reagent (Thermo Fisher Scientific). Z-stacks were acquired by inverted epifluorescence microscope (Zeiss AxioObserver.Z1/7, Carl Zeiss, Oberkochen, Germany) with Zeiss ApoTome additional feature. The Plan-Apochromat 40×/0.95 Korr M27 objective was used and digital images of 16 bit were acquired with a 0.163 μm × 0.163 μm × 1.000 μm voxel size, using 4.2 Megapixel monochrome sCMOS camera (Orca-flash 4.0 V2, Hamamatsu Photonics, Hamamatsu, Japan). Each z-stack, containing 10–20 images, was acquired in three excitations wavelengths (633, 493, and 353 nm) and exposure with 1.9 s, 16 ms, and 300 ms. Post-processing of the resulting z-stack files was performed with Fiji version 1.52p.[29]

Measurement of the volume of isolated cardiomyocytes

The following image processing workflow was carried out to the image processing software Fiji (version 1.52p).

From the resulting hyperstack, the channel representing the Alexa Flour 488 Phalloidin signal was extracted as 3D greyscale image stack. Binarization was done by choosing a grey value threshold excluding most of unwanted background signal. Adjacent areas were closed by performing a morphological closing operation 1 to 5 times with a 1 count square structuring element. Small speckles (max. radius 2–20 pixels), which were falsely assigned as foreground were removed with the 'remove outliers'-function. The resulting areas were analysed with the 'analyse particles' tool, assuming a circularity of 0.0–0.7 for each area. The resulting areas on each slide were multiplied by the slice thickness and summarized to get the volume of each cell.

Transmission electron microscopy/focused ion beam-scanning electron microscopy tissue preparation

For TEM and FIB-SEM analysis of mouse LV tissue, heart specimens were prepared in a similar way. Explanted mouse

hearts were rapidly dissected into small slices and transferred into a petri dish filled with primary fixative (<20 s, 2% formaldehyde, 2.5% glutaraldehyde and 2 mM $CaCl_2$ in 0.15 M cacodylate buffer). Biopsies of 1 mm^3 were collected in a 1.5 mL tube (Eppendorf, Hamburg, Germany) filled with the same primary fixative. After fixation (3 h, RT), the biopsies were rinsed three times with 0.15 M cacodylate buffer, followed by post-fixation and contrasting according to a modified protocol of the OTO method.[30] Subsequently, specimens were dehydrated in an ascending ethanol gradient (30%, 50% 60%, 70%, 80%, 96% and three times 100%; each step 15 min) and embedded in Durcupan™ with an incrementally increasing resin concentration (2× pure propylene oxide (PO) for 2 min, followed by Durcupan™: PO 1:1 (1 h) and 3:1 (1.5 h) at RT, and finally pure Durcupan™ first overnight (O/N) and then freshly refilled with pure Durcupan™) followed by polymerization for 72 h at 60°C.

Isolated cardiomyocytes from adult mice were cultured for 2.5 h after seeding and fixed in 2.5% glutaraldehyde for 3 h. Post-fixation and contrasting process were performed as described earlier for heart specimens. The following steps of the process were modified: phosphate-buffered 1% osmium tetroxide for 30 min on ice and 0.5% aqueous solution of uranyl acetate without Walton's lead aspartate staining. Instead of Durcupan embedding, EPON with an incrementally increasing resin concentration (EPON:EtOH 1:1 [1 h] and 3:1 [2 h] at RT), and then pure EPON O/N was used. The resin was then polymerized at 60°C for 48 h before the glass bottom of the dish was removed by incubation in 40% hydrofluoric acid for 30 min at RT.

Human heart biopsy was immediately transferred to a 1.5 mL tube, containing primary fixative as described earlier and processed as described for mouse LV tissue.

Transmission electron microscopy images

Ultrathin sections of heart specimens (55 nm) were generated (EM UC7, Leica)[31] and transferred to 200 mesh copper grids. Imaging was conducted using a LaB6 cathode-equipped JEM 1400Plus (JEOL, Ltd., Tokyo Akishima, Japan) instrument at 120 kV with magnifications as indicated. Digital images were acquired with a CMOS camera with 4096 × 4096 pixels (TemCam-F416, TVIPS, Gauting, Germany). Post-processing of the resulting 8-bit TIFF image files was performed with Fiji version 1.52p.[32]

Focused ion beam-scanning electron microscopy and data acquisition

The resin disc containing isolated myocytes were trimmed with a scalpel to a macroscopically chosen region approximately 1 cm in diameter and glued onto an SEM aluminium stub using conductive silver paste (Plano GmbH, Wetzlar, Germany). The embedded tissue was cut off the resin block with a razor blade and was also glued onto an SEM aluminium stub. The surface was then coated with a 15 nm-thick platinum/palladium layer (208HR, Cressington Scientific Instruments, Watford, UK) before the stub was transferred into the FIB-SEM (Crossbeam 540, Carl Zeiss AG) column for O/N vacuum stabilization. The embedded sample was screened for representative cells using the SmartSEM software package (Carl Zeiss AG, version 6.04) at an accelerating voltage of 1.5 and 10 kV and a beam current of 1 nA (working distance, 5.1 mm; analytic column mode; 164 × magnification, Everhart-Thornley detector). A coarse trench was milled directly in front of the region of interest (ROI) using the FIB at 30 kV/65 nA and the SmartFIB software package (Carl Zeiss AG, version 1.8.0). For 3D image acquisition of isolated myocytes, the Atlas System (Carl Zeiss AG; software version 5.2.2.85) was used while the system operated at the following parameters: gallium ion beam: 30 kV/30 nA, electron beam: 1.5 kV/1 nA, field of view: 97.8 μm, cutting thickness: 100 nm, pixel size: 8.1 nm and pixel dwell time: 3.5 μs. Eight-bit TIF images were acquired using both a column energy selective backscatter detector with a 700 V energy selective backscatter grid and an S1-selective in-lens detector at a resolution of 12 032 × 12 032 pixels.

For heart tissue, a 40 × 20 μm protection pad was additionally generated with SmartFIB using a gas injection system (gallium ion beam: 30 kV/3 nA). Image acquisition was performed with the following parameters: gallium ion beam: 30 kV/3 nA, electron beam: 1.5 kV/1 nA, field of view: 30 μm, cutting thickness: 150 nm, pixel size: 2 nm, and pixel dwell time: 10 μs.

Three-dimensional reconstructions

Subsequent image processing was carried out by a combination of various computer programs. Image brightness and contrast adjustment, image stack alignment, image inversion, and image/stack cropping were performed using either Atlas or Amira (Thermo Fisher Scientific, Inc., Waltham, MA, USA; version 2019.4). Segmentation of the cellular ultrastructure was performed using either the magic wand or the brush tool of Amira on all consecutive images of one stack. Amira was also used for 3D reconstruction and the generation of parameters, such as volume, shape, and number, for quantitative analyses. Fiji was used to generate rendered 3D movies from the TIF series, initially composed in Amira.

Isolation of mitochondria

The isolated mouse heart was disrupted in 2 mL of ice-cold isolation buffer (250 mM sucrose, 10 mM HEPES, and 1 mM

EGTA, pH 7.4) using a TissueRuptor.[33] The homogenate was centrifuged (700 × *g* for 10 min at 4°C) to remove debris. Then, the supernatant was centrifuged at an increased speed (15 000 × *g* for 10 min at 4°C) to precipitate mitochondria. The mitochondria were washed twice with isolation buffer through resuspension and centrifugation at 12 500 × *g* for 5 min at 4°C. Finally, the mitochondria were resuspended in 300 μL of isolation buffer. The total protein concentration was measured by DC Protein Assay (Bio-Rad Laboratories, Inc., Hercules, CA, USA) according to the manufacturer's instructions. The measured protein concentration was used to determine the total number of mitochondria per heart.

Mitochondrial respiration

Based on the protein quantification, the mitochondrial suspensions, isolated mitochondria from WT (*n* = 5) and *Bnip3*$^{-/-}$ mice (*n* = 5) were diluted to the working concentration of 4 μg/mL total protein with cold 1× mitochondrial assay solution (MAS) (2 mM HEPES, 10 mM KH_2PO_4, 220 mM mannitol, 1 mM EGTA, 70 mM sucrose, 5 mM $MgCl_2$, 0.2% fatty acid-free bovine albumin serum (BSA), pH 7.2) supplemented with 10 mM succinate and 2 μM rotenone. The wells of an XF24 V7 PS 24-well cell culture microplate[34] (Agilent Technologies, Santa Clara, CA, USA) were loaded with five replicates of 50 μL of diluted mitochondria suspension (2 μg protein/well). For background correction, the corners were filled with only 1 × MAS. The microplate was centrifuged for 20 min at 2000 × *g* at RT to attach the mitochondria to the bottom of the plate. Finally, 450 μL of pre-warmed (37°C) 1 × MAS was added to each well. During centrifugation, the ports of an XFe24 cartridge were filled as follows: port a: 55 μL of 40 mM adenosine diphosphate, port b: 62 μL of 25 μg/mL oligomycin, port c: 69 μL of 40 μM carbonyl cyanide 4-(trifluoromethoxy) phenylhydrazone (FCCP), port d: 75 μL of 40 μM antimycin A. The oxygen consumption rate was then detected with a Seahorse XF24e Analyser (Bioscience, North Billerica, USA). The software suite WAVE (Agilent Technologies; version 2.6.0) was used for data analysis.

Western blot analysis

After the isolation of mitochondria and homogenization of whole hearts, the protein concentration was determined by DC Protein Assay (Bio-Rad Laboratories Inc., Hercules, CA, USA). Samples were diluted in lithium dodecyl sulfate sample buffer and Reducing Agent (Invitrogen, Carlsbad, CA, USA) and boiled for 5 min at 95°C. The denatured samples were loaded onto NuPAGE™ 4–12% Bis-Tris protein gels (Invitrogen). Then, the proteins were transferred to nitrocellulose membranes and stained with SYPRO Ruby (Thermo Fisher Scientific, USA) following the manufacturer's instructions. Subsequently, non-specific binding sites were blocked, and the blots were subjected to primary antibody incubation overnight at 4°C. After exposure to the horseradish peroxidase (HRP)-conjugated secondary antibody for 1 h at RT, the blots were imaged using SuperSignal West Pico PLUS Substrate (Thermo Fisher Scientific, USA).

Antibody list

Antibody	Host	Manufacturer (catalogue number)
Actin	Mouse	MP Biomedicals (691001)
Anti-rabbit-HRP	Goat	Cell Signaling (7074)
Anti-OMA-1	Rabbit	Cell Signaling (95473)
Anti-OPA-1	Rabbit	Cell Signaling (80471)

Echocardiography

A high-frequency ultrasound system (Vevo 3100, FUJIFILM VisualSonics, Toronto, Canada) was used to acquire ultrasound images. An MX400 38 MHz (21–44 MHz) transducer with up to 449 fps and an image axial resolution of 50 μm was used (FUJIFILM VisualSonics). Mice were anaesthetized using 3% isoflurane initially. Anaesthesia was maintained with 1.5–2% isoflurane with a 100% dioxygen flow of 1–2 L/min.[35,36] The animals were placed in the supine position and taped to a heated electrocardiogram table to record electrocardiogram signals. Body temperature was monitored *via* a rectal thermometer and maintained using infrared light. Hair was removed using a chemical depilatory agent. 2D B- and M-mode cine loop images were acquired in the parasternal long (PSLAX) and parasternal short-axis (SAX) view as well as the apical four-chamber (4CH) view.[37,38] M-mode images in the SAX view were recorded at the mid-papillary LV level. Conventional analysis of the images as well as strain analysis was performed in a blinded manner using Vevo LAB software version 3.2.2 (FUJIFILM VisualSonics) and Vevo Strain software (FUJIFILM VisualSonics), respectively. Fractional shortening was calculated based on strain analysis.

Quantification and statistical analysis

Samples from three mice per genotype (WT and *Bnip3*$^{-/-}$) were included. From each mouse, one biopsy was taken, and four randomly chosen FIB-SEM stacks were recorded. One image stack from a *Bnip3*$^{-/-}$ mouse was excluded because it contained only 11 mitochondria and hence was not representative. In summary, 729 mitochondria from WT mice and 1285 mitochondria from *Bnip3*$^{-/-}$ mice were analysed. The spatial parameters of the cellular compartments and, in particular, of the mitochondria (area, volume, and perimeter) were calculated using Amira software (version 2019.4).

Mitochondrial complexity was described through the mitochondrial complexity index (MCI), which was developed by Koopmann *et al*. and adapted by Vincent *et al*.[39,40] The following formula was used:

$$\mathrm{MCI} = \left(\frac{\left(SA^{3/2}\right)}{4\pi V}\right)^2 = \frac{SA^3}{16\pi^2 V^2}$$

with *SA* as the surface area, and *V* as the volume.

The following mitochondrial shape parameters were calculated using Amira software. As described in the user's manual, anisotropy (a), elongation (e), and flatness (f) were derived from the eigenvalues and eigenvectors given by the inertia tensor of the segmented mitochondria. The formula for anisotropy was one minus the ratio of the smallest to the largest eigenvalue. Elongation was calculated as the ratio of the medium to the largest eigenvalue. Flatness was derived from the ratio of the smallest to the medium eigenvalue. The final conclusion regarding mitochondrial shape was made through the collective consideration of these parameters. To illustrate how each single parameter describes the mitochondrial shape, we used representative mitochondria and formed the corresponding ellipsoids from the resulting *x*, *y*, and *z* eigenvalues.

Corresponding to the observed shapes from 3D recalculations, all segmented mitochondria were considered globular (r: 0–0.4; e: 0.6–1; f: 0.6–1), rod-shaped (r: 0.6–1; e: 0–0.4; f: 0.5–1), long-striped (r: 0.8–1; e: 0–0.4; f: 0–0.4), flattened (r: 0.6–1; e: 0.5–1; f: 0–0.4), or soft square-shaped (r: 0.5–1; e: 0.5–1; f: 0.5–1). Therefore, we used a custom python script (Supplementary Listing S1).

For statistical testing and the generation of graphs, Prism 8 software was used (GraphPad, San Diego, CA, USA). Data are presented as the mean ± SD. For each group, the Shapiro–Wilk test was performed (normal distribution). If normally was assumed, comparisons were performed using Student's *t* test. Otherwise, data were analysed by the Mann–Whitney test. The correlation coefficients and determination coefficients were calculated using the Pearson method. To compare multidimensional parameters, root extraction was performed. Skewness and kurtosis were extracted by heuristic prism analysis (GraphPad Software, San Diego, CA, USA, version 8.4.3). These parameters show how much a given distribution deviates from the normal distribution (Gaussian distribution). While skewness describes deviations in terms of symmetry, kurtosis describes deviations in terms of steepness. An increasing absolute skewness reflects a more asymmetrical distribution. A positive value represents a peak shift to the left, whereas a negative value reflects a peak shift to the right. In contrast, high kurtosis indicates an increased value number at the edges (tails). Thus, kurtosis describes how flat or steep the distribution curve appears. A negative kurtosis indicates a flat distribution with short tails. Such distributions are also called platykurtic.[41]

Results

Overall workflow

For the reliable and efficient analysis of mouse cardiac tissue biopsies, we established the following workflow (*Figure* 1), based on a published 3D SBF-SEM protocol.[42] Cubic cardiac biopsies with an edge length of 1 mm were collected from the left ventricle of adult mouse hearts (*Figure* 1A) and immediately immersion-fixed with aldehyde. To enhance the sample contrast, we used five different heavy metals during sample processing before embedding the biopsies (*Figure* 1B). From the resin blocks, semi-thin sections were cut to identify representative ROIs (*Figure* 1C) around which the blocks were then coarsely trimmed. Finally, FIB-SEM was performed to analyse the mitochondria inside the cardiac tissue. For these analyses, single volumes of 10 × 10 × 3.15 μm (*x*–*y*–*z*) were recorded at a voxel size of 2 × 2 × 150 nm, which resulted in 21 individual image planes per volume (*Figure* 1D,E). This setting allows to fully record the variations of the mitochondrial size while preserving the mitochondrial ultrastructure. A representative example of such an image stack is depicted in *Figure* 1E. In the upper row of *Figure* 1F, two images from this stack (the first = top and the last = bottom) are shown, whereas the row below represents the corresponding segmentation maps of the mitochondria. For the accurate quantification of mitochondrial features, all mitochondria were segmented manually on each section of the z-stack. Because manual segmentation, in particular related to the surface area, depends on individual hand movements of the person tracing, intra-individual and inter-individual variability with a coefficient of variation less than 10% is recommended. Finally, 3D rendering and parameter analyses were carried out using a combination of different software tools. *Figure* 1G shows a visualization of the resulting 3D model of the example data set. The entire workflow is summarized in *Figure* 1H. The cardiomyocytes were processed for FIB-SEM as were the cardiac tissues with only minor changes, which are listed in the Methods section. This workflow is instantly adaptable to laboratories that have access to any of the FIB-SEM, SBF-SEM, or array tomography (serial sectioning) instruments.

Three-dimensional mapping of mitochondria in isolated cardiomyocytes and cardiac tissue

In the resulting 3D model of a representative isolated cardiomyocyte, the mitochondrial reticular network appeared to be mostly arranged in a linear manner between the myofibrils (*Figure* 2A). Moreover, as shown in the cross-sections, mitochondria aggregated in proximity to the nucleus (*Figure* 2B,C). 3D mapping of this cardiomyocyte revealed that

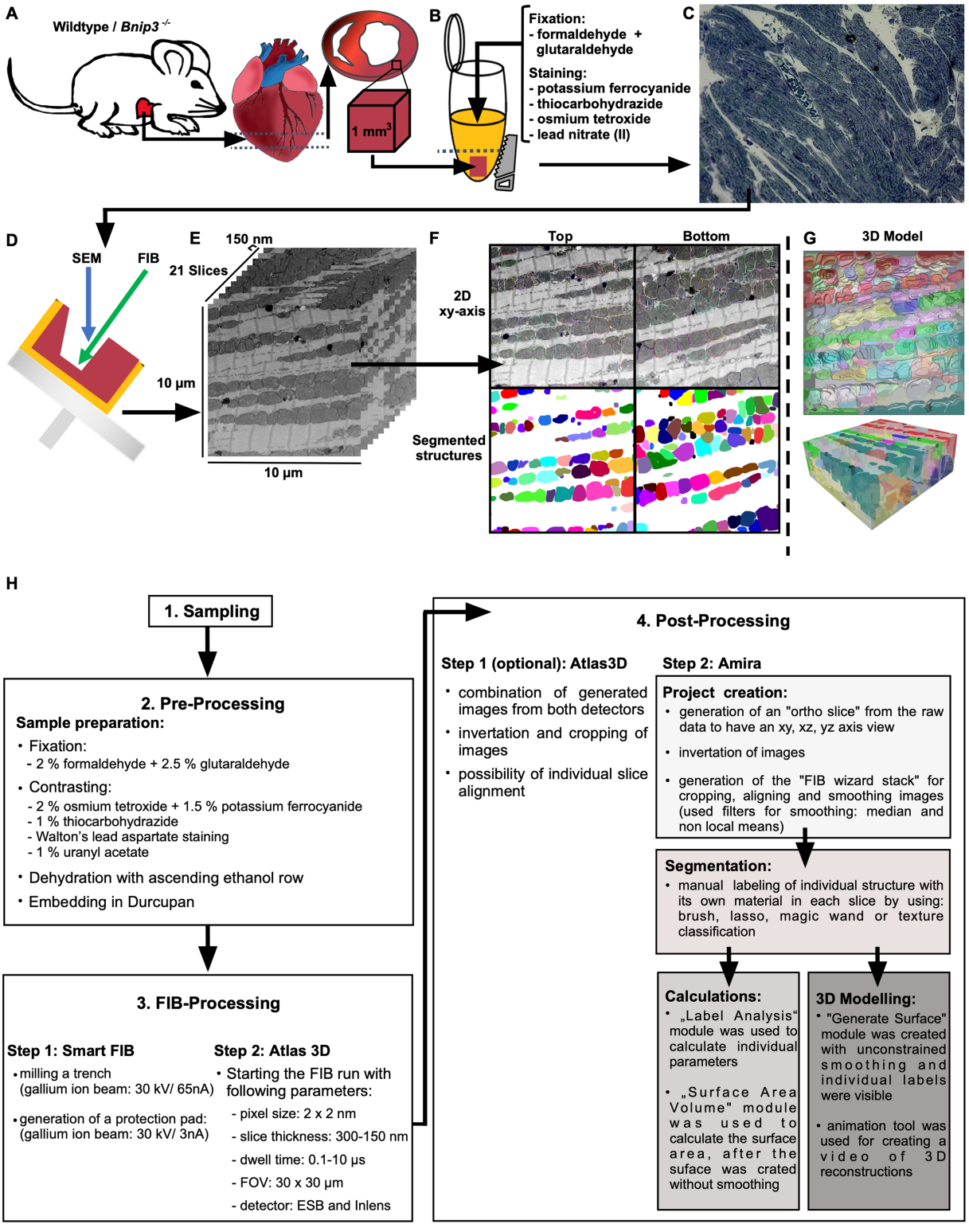

Figure 1 Workflow. (*A*,*B*) schematic diagram of sample acquisition and preparation for focused ion beam-scanning electron microscopy (FIB-SEM) (n = 3 mice per group). (*C*) Representative light micrograph of a semi-thin section used to identify the regions of interest (ROIs). (*D*) Schematic of the FIB-SEM process illustrating cutting and imaging. (*E*) Z-stack of two-dimensional (2D) images from FIB-SEM with an imaging depth of 3.15 µm. (*F*) Top and bottom images of the z-stack and the corresponding segmentation maps of mitochondria. Each fully mapped mitochondrion is represented by a colour. (*G*) Three-dimensional (3D) reconstruction representing segmented mitochondria. (*H*) Flow chart indicating the significant steps of sample processing.

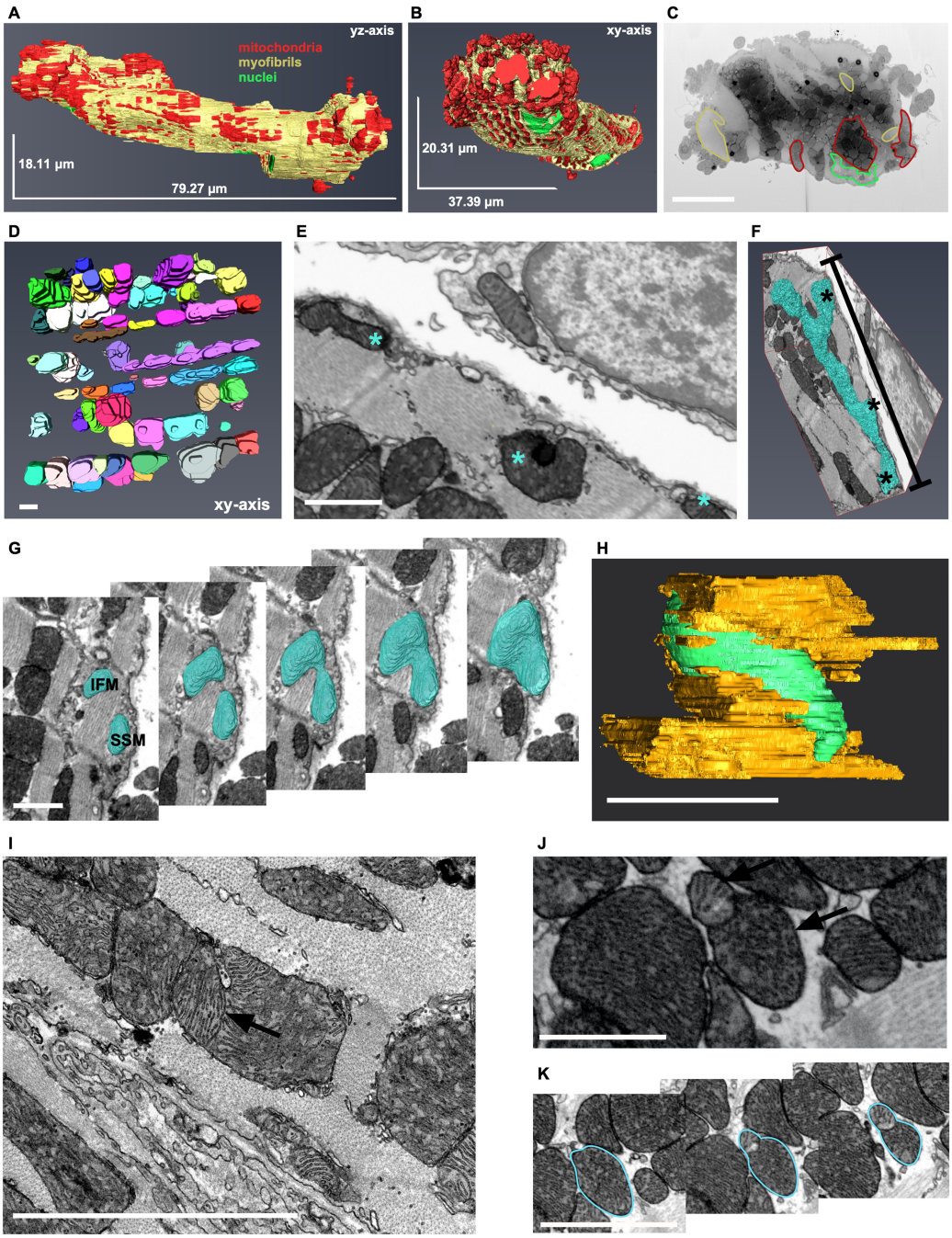

Figure 2 Three-dimensional (3D) mapping of mitochondria in isolated cardiomyocytes (n = 3 from 1 mice) and cardiac tissue. (*A*,*B*) 3D reconstructions of a longitudinally (*A*) and transversally (*B*) oriented isolated mouse cardiomyocyte with mitochondria highlighted in red, myofibrils in yellow and nuclei in green. Refer to Supporting information, *Movie* S1 for animation. (*C*) Electron micrograph of an isolated cardiomyocyte in a transverse orientation. Scale bar, 5 µm. (*D*) 3D reconstruction of the cardiomyocyte mitochondrial network in cardiac tissue (n = 3 wild-type mice, each with four z-stacks). Each mitochondrion is represented by a different colour. Scale bar, 1 µm. Refer to *Movie* S2 for animation. (*E*,*F*) two-dimensional (2D) image depicting three separate mitochondria (*E*, asterisks). Note that the 3D reconstruction reveals merely one complex mitochondrion up to 6 µm with two branches (*F*, cyan). Scale bar, 1 µm (1 wild-type mouse, n = 1 z-stack). Refer to *Movie* S3 for animation. (*G*) Z-stack images obtained by focused ion beam-scanning electron microscopy (FIB-SEM) (cyan) depicting disparate parts of the same mitochondrion, appearing as one subsarcolemmal (SSM) and one interfibrillar (IFM) mitochondrion in one single 2D section. Scale bar, 1 µm (1 wild-type mouse, n = 1 z-stack). Refer to *Movie* S4 for animation. (*H*) 3D reconstruction of a single mitochondrion (green) extending across a myofibril bundle (yellow). Scale bar, 1 µm (1 wild-type mouse, n = 1 z-stack). Refer to *Movie* S5 for animation. (*I*) 2D transmission electron microscopy (TEM) image depicting fragmented mitochondria (black arrows). Scale bar, 3 µm (1 wild-type mouse, n = 1 z-stack). (*J*) 2D image depicting two individual mitochondria (black arrows). (*K*) Z-stack images obtained by FIB-SEM illustrating fission. Scale bar, 3 µm (1 wild-type mouse, n = 1 z-stack). Refer to *Movie* S6 for animation.

mitochondria accumulated at distal cell boundaries on the *z*-axis, whereas fewer mitochondria were detected in the centre of the cell (Supporting information, *Movie* S1). In addition, they showed a more dispersed arrangement on the x-y plane than those in intact cardiac tissue.[43] This different organelle arrangement could be due to the isolation process followed by cultivation in an artificial cell culture dish. Therefore, mitochondria might adapt their spatial distribution according to the physiological demand within the isolated cardiomyocyte.

As the isolation and cultivation process leads to an artificially altered distribution of mitochondria within the cardiomyocyte, we evaluated intact LV tissue. Depicting only the mitochondrial network of the cardiomyocyte, the complex shape and size of mitochondria became obvious (*Figure* 2D, *Movie* S2). The mitochondrial appearance varied from spherically round to elongated and from uniform to polymorph shapes. The linear arrangement of the mitochondria was clearly connected to the spatial course of the myofibrils. Along the course of myofibrils, a preference for elongation was detected (*Figure* 2D, *Movie* S2).

The heterogeneous appearance of the cardiomyocyte mitochondria indicates that an analysis of single 2D images from a z-stack was prone to misinterpretation regarding the mitochondrial number, localization, and dynamics. As depicted in *Figure* 2E,F mitochondria that appeared as distinct organelles with different shapes located in either subsarcolemmal (SSM) or interfibrillar (IFM) regions in the 2D plane turned out to be one and the same mitochondrion when 3D analyses were applied. Moreover, the 3D volume revealed that this elongated mitochondrion branched and was present in the interfibrillar and subsarcolemmal regions (*Figure* 2E,F, *Movie* S3). In a previous study, we had already challenged the concept that IFM and SSM generally belong to different mitochondrial subpopulations[43] and can provide here the ultimate proof of our hypothesis. Another example with a high likelihood of such a misinterpretation is shown in *Figure* 2G (*Movie* S4). Two mitochondria separated by a myofibril bundle could easily be described as IFM and SSM on 2D examination, but in reality, they turned out to be one mitochondrion present in both compartments. This phenomenon can be explained by the fact that mitochondria are able to cross myofibril bundles, as shown in *Figure* 2H, where the elongated mitochondrion (green) bypasses the cardiac myofibril bundle (yellow) (*Figure* 2H, *Movie* S5). Another drawback of 2D analysis applies to the examination of fragmented mitochondria during the fission process. Whereas in *Figure* 2I the demarcation line of fission is apparent, *Figure* 2J even suggests the existence of two individual mitochondria. Assembling the z-stack into a 3D model, however, unmasked the fission process of one mitochondrion (*Figure* 2K, *Movie* S6).

Quantitative two-dimensional analyses of cardiomyocyte mitochondria cannot reflect the real situation in three-dimensions

Because the 3D analysis of cardiac tissue (*Figure* 2) impressively unmasked the heterogeneity of cardiomyocyte mitochondria in size, shape and distribution, we focused on the question of whether classical 2D analyses can reflect the outcome of 3D quantifications. To allow proper comparison of the parameters describing the relative values of number, size and shape of individual mitochondria and coverage area of mitochondria, we compared 12 3D reconstructions of LV specimens totalling 315 μm^3 with 12 2D intersections (10 × 10 μm). Here we used the 12 z-stack top and bottom intersections. To reveal whether a linear association existed for mitochondrial number and coverage space between the 2D values and 3D results, we calculated the Pearson correlation coefficient (r) and the determination coefficient (r^2) for 12 corresponding samples. Because r was close to zero, no correlation for mitochondrial number could be confirmed (*Figure* 3A; top section: $r = 0.02$, $r^2 = 0.004$, $P = 0.9511$ and bottom section: $r = -0.06$, $r^2 = 0.004$, $P = 0.8466$). Furthermore, r^2 showed that only 4% of the difference in the 2D values was accounted for by the difference in the 3D values. This was not surprising because the 2D data deviated from the 3D results by up to 66% (*Figure* S1A; top section 66% and bottom section 57%). A low r was also calculated for the mitochondrial dispersion space, which indicated no linear relationship between data obtained by 2D and 3D analysis (*Figure* 3B; top section: $r = -0.03$, $r^2 = 0.001$, $P = 0.9188$ and bottom section: $r = -0.51$, $r^2 = 0.255$, $P = 0.0936$). Here, the deviation in the 2D data reached 395% (*Figure* S1B; top section 338% and bottom section 395%). Related to r^2, only 26% of the variation in the 3D results was represented in the 2D data. Overall, 2D analyses generally do not predict the corresponding proportions that exist under 3D conditions in terms of mitochondrial number or coverage space.

Alterations in mitochondrial size and shape have been reported as hallmarks of many pathologies, including heart failure, and have been attributed to impaired mitochondrial dynamics.[44–46] To verify these reports, we next evaluated the size of individual mitochondria in 2D and 3D and analysed the resulting populations using cumulative frequency distribution calculations. In 3D, size corresponds to volume, whereas in 2D, size equals an area. To avoid a bias in direct comparison, the value dimensions (μm^2 and μm^3, respectively) were removed through the extraction of their roots. The cumulative frequency distributions illustrated a diverse abundance of mitochondria with different sizes in 3D and 2D (*Figure* 3C). Hence, we consider that size determination depends on the observation dimension. To confirm this presumption, we focused on the symmetry and tailedness of

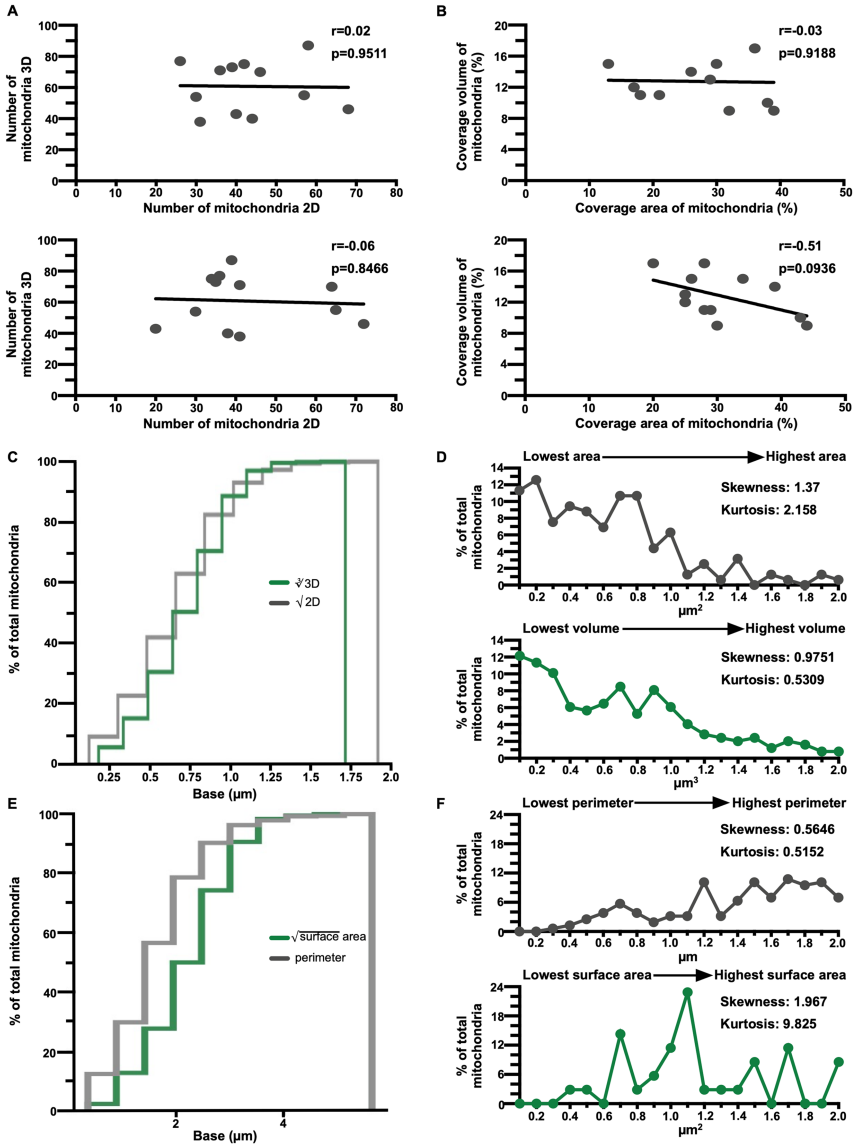

Figure 3 Quantitative two-dimensional (2D) analyses of cardiomyocyte mitochondria cannot reflect the real situation in three-dimensional (3D). (*A*) Mitochondrial number in 3D reconstructions and corresponding 2D top (upper panel) and bottom sections (lower panel) from 12 focused ion beam-scanning electron microscopy (FIB-SEM) stacks (n = 3 wild-type mice). Pearson analysis does not prove a linear correlation. Refer also to Supporting information, *Figure* S1A. (*B*) Mitochondrial coverage volume and area from 12 FIB-SEM stacks and corresponding 2D top (upper panel) and bottom sections (lower panel) (n = 3 wild-type mice). Pearson analysis does not prove a linear correlation. Refer also to *Figure* S1B. (*C*) Cumulative frequency distribution of individual mitochondrial size in 3D and 2D (top section) (n = 3 wild-type mice, 12 z-stacks). In 3D, size is indicated by the mitochondrial volume (green), and in 2D, size is indicated by the mitochondrial area (grey). The roots of absolute values were extracted. Refer also to *Figure* S1C. (*D*) Representative histograms of individual mitochondrial size. The mitochondrial surface area frequency in the top section of four FIB-SEM stacks is shown in the upper panel (grey), and the corresponding volume frequency in the 3D reconstruction is shown in the lower panel (green) (n = 1 wild-type mouse). (*E*) Cumulative frequency distribution of individual mitochondrial shape parameters in 3D and 2D (top sections) (n = 3 wild-type mice, 12 z-stacks). In 3D, the shape is indicated by the mitochondrial surface area (green), and in 2D, it is indicated by the mitochondrial perimeter (grey). The roots of absolute values were extracted. Refer also to *Figure* S1D. (*F*) Representative histograms of individual mitochondrial shapes (n = 1 wild-type mouse). The mitochondrial perimeter frequency in the top section of four FIB-SEM stacks is shown in the upper panel (grey), and the corresponding surface area frequency in the 3D reconstruction is shown in the lower panel (green).

the size distribution. In this respect, we calculated skewness and kurtosis. These population distribution values differed in histograms of four 3D volumes and their corresponding 2D top intersections (*Figure* 3D; skewness 1.37 vs. 0.9751; kurtosis 2.158 vs. 0.5309) and 2D bottom intersections (*Figure* S1C,D; skewness 1.446 vs. 0.9751; kurtosis 3.593 vs. 0.5309). From these data, a 2D analysis was suggestive of a more asymmetric and leptokurtic size distribution with a shift to smaller size values overall compared with a 3D analysis. Mitochondrial shape could be determined by connecting

perimeter (2D) and surface area (3D) data with size properties. Therefore, we next compared these parameters in 2D and 3D analyses. Here, we adjusted surface areas by extracting roots to create comparability with perimeters. Cumulative frequency distribution comparison suggested a diverse but overall increased abundance of mitochondria with a larger perimeter than the corresponding 3D descriptor surface area (*Figure* 3E). Additionally, the distribution symmetry and tailedness of the surface area and perimeter appeared asymmetric, with heavier tails on 3D than 2D analysis (*Figure* 3E), which was apparent in histograms of four 3D volumes and their corresponding 2D top intersections (*Figure* 3F; skewness 0.5646 vs. 1.967; kurtosis 0.5152 vs. 9.825) and 2D bottom intersections (*Figure* S1E,F; skewness 0.8319 vs. 1.967, kurtosis 1.824 vs. 9.825).

Next, we tested whether the assessment of mitochondrial shape differs between an experimental 2D and 3D approach using anisotropy and elongation scores. Anisotropy values close to zero represented a rounder object, whereas elongation values close to zero represented a more elongated object (*Figure* 4A). Correlation analyses of 12 3D reconstitutions with their corresponding top and bottom 2D intersections did not show a relationship between the number of mitochondria with a round shape (anisotropy: 0–0.4) (*Figure* 4B; top: $r = 0.15$; $r^2 = 0.023$; $P = 0.6397$; bottom: $r = 0.09$; $r^2 = 0.008$; $P = 0.7839$). This also applied to the number of elongated mitochondria (elongation: 0–0.4) (*Figure* 4C; top: $r = -0.09$; $r^2 = 0.008$; $P = 0.7804$; bottom: $r = -0.09$; $r^2 = 0.008$; $P = 0.7758$). Quantifying mitochondria at the aggregated level within the 12 3D volumes and 12 2D slices revealed a markedly different rating of shape abundance and variety (*Figure* 4D). Compared with the number of round mitochondria identified by 3D mapping, the number of mitochondria counted as round by 2D analysis was 4.5-fold higher (top section: 31% *vs*. 7%, bottom section: 32% *vs*. 7%). Elongated mitochondria were 50% more abundant on 3D than 2D analysis (top section: 93% vs. 69%; bottom section: 93% vs. 68%).

These data clearly indicate that a 2D observation is inadequate to reflect cardiomyocyte mitochondrial characteristics with respect to number, coverage area, and shape. To properly evaluate the mitochondrial parameters and to understand the relationships between mitochondrial morphology and physiology in cells displaying a substantial 'thickness' in the axial (*z*) direction, as do cardiomyocytes, 3D image analysis is indispensable.

BNIP3 deletion leads to alterations in mitochondrial number and dispersion

As shown earlier, for proper comparison of the mitochondrial compartment between physiological and pathological conditions, ultrastructural 3D characterizations are of crucial importance. FIB-SEM was subsequently performed to identify the role of BNIP3 under natural conditions *in situ* using genetically modified mice deficient in this protein.[26]

From 2D image material obtained by FIB-SEM as well as conventional TEM analyses, we gained the impression that mitochondria were more abundant in the LV tissue of *Bnip3*$^{-/-}$ mice (*Figure* 5C,D) than WT mice (*Figure* 5A,B). In the cardiomyocytes of the *Bnip3*$^{-/-}$ mice, mitochondria formed large clusters between the myofibril bundles, and they filled a large portion of the cardiomyocyte area (*Figure* 5C,D). The cardiomyocytes of the *Bnip3*$^{-/-}$ mice seemed to have a decreased dispersion of actin bundles, and most of the mitochondria displayed a round shape (*Figure* 5C,D). In these 2D analyses, no obviously damaged mitochondria were found in the *Bnip3*$^{-/-}$ mice (*Figure* 5C,D,F), and their mitochondrial ultrastructure was comparable with that in their WT counterparts (*Figure* 5A,B,E). Furthermore, alterations in neither the spatial distribution nor the morphology of the sarcoplasmic reticulum or the T-system were detectable (*Figure* 5E,F), and morphological features of impaired mitophagy could not be found in cardiomyocytes lacking BNIP3 expression.

As we have shown that such a classical 2D TEM analysis of cardiac cells is generally prone to data misinterpretation and therefore might deliver debatable results, we next aimed to verify our subjective 2D description by a comparative, quantitative 3D FIB-SEM approach. The first, again, just qualitative impression, we gained from the resulting 3D mappings was the formation of dense mitochondrial clusters in different areas/volumes of the investigated cell (*Movie* S7). Then, we addressed the number of mitochondria and, in parallel, the mitochondrial and fibrillar coverage in 315 μm^3 volumes of LV tissue. For the WT mice, we found an arithmetic average of 212 mitochondria inside the analysed volume (=0.67 mitochondria/μm^3; *Figure* 5G), which covered on average 128 μm^3 (*Figure* 5H) and therefore accounted for approximately 41% of the total observed volume. Among these organelles counted in the 'total number', many mitochondria were located at the outer borders of the volume and were not acquired as completely closed organelle bodies. As shown earlier, there is a certain likelihood that such incompletely acquired mitochondrial structures ultimately fuse in non-visible 3D planes to become one and the same organelle. To take this source of error risk into account, we also analysed the tissue volume for just fully acquired, closed mitochondrial bodies. In the WT mice, we thereby assessed an average number of 61 mitochondria (=0.19 mitochondria/μm^3; *Figure* 5I) occupying 40 μm^3 of the analysed volume (*Figure* 5J), which accounted for approximately 13% of the 315 μm^3. Inside the investigated *Bnip3*$^{-/-}$ sample volumes, a total of 359 mitochondria were counted on average (=1.14 mitochondria/μm^3; *Figure* 5G), accounting for 167 μm^3 = 53% of the total tissue volume (*Figure* 5H). Counting only fully acquired organelle bodies, an average number of 117 mitochondria (=0.37

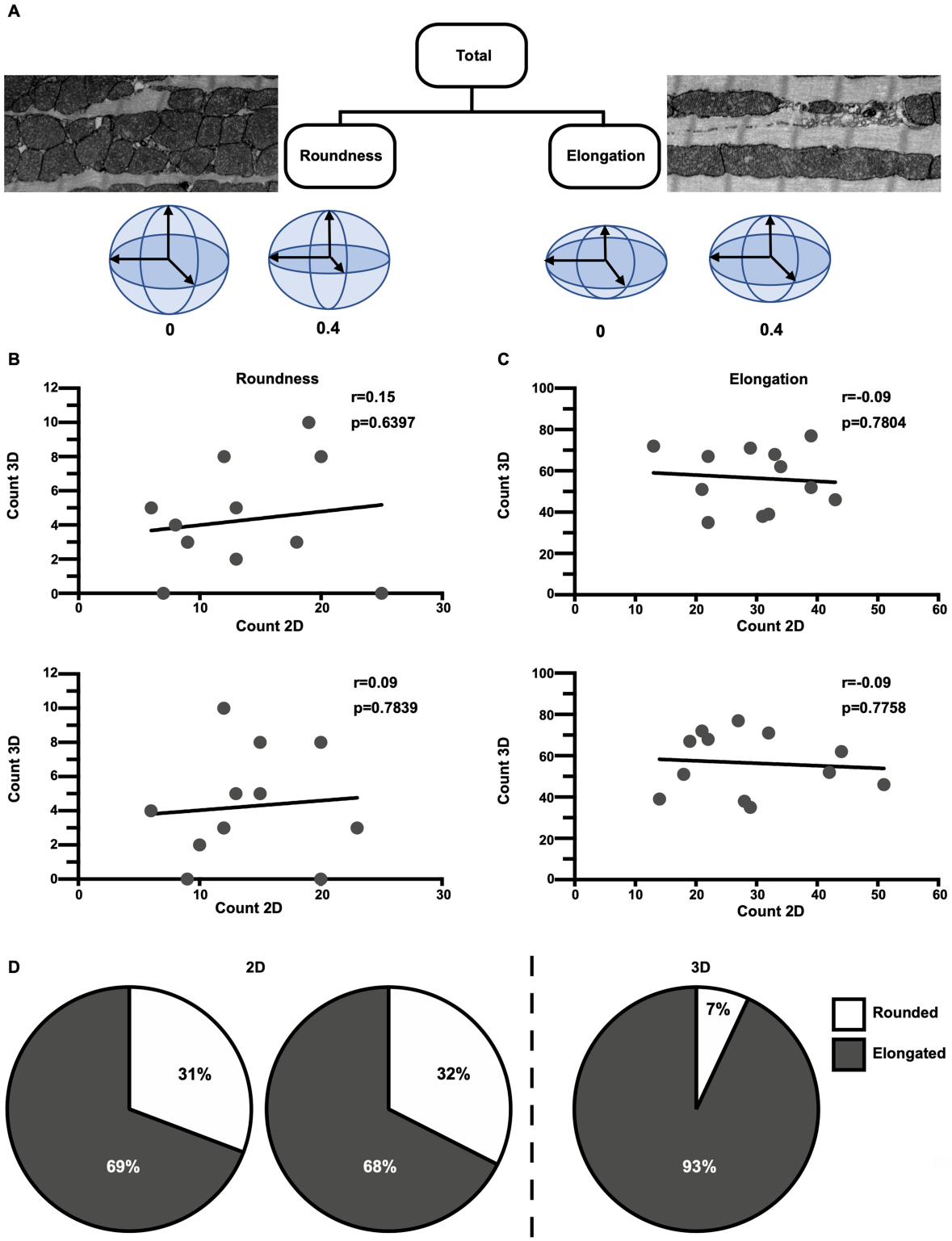

Figure 4 Quantitative two-dimensional (2D) analyses do not reflect three-dimensional (3D) facts in terms of shape. (*A*) Assessment scheme for mitochondrial shape. The anisotropy score was used to assign mitochondria to the 'rounded' group (≤0.4; left side), and the elongation score was used to assign mitochondria to the 'elongated' group (≤0.4; right side). (*B*,*C*) Mitochondrial shape divided according to 'roundness' (*B*) and 'elongation' (*C*) in the 3D reconstructions and corresponding 2D top (upper panel) and bottom sections (lower panel) from 12 focused ion beam-scanning electron microscopy (FIB-SEM) stacks (*n* = 3 wild-type mice). Pearson analysis does not prove a linear correlation. (*D*) Proportions of the mitochondrial shapes in the top and bottom sections (2D, left panel) and 3D reconstructions (right panel) of 12 FIB-SEM stacks (*n* = 3 wild-type mice).

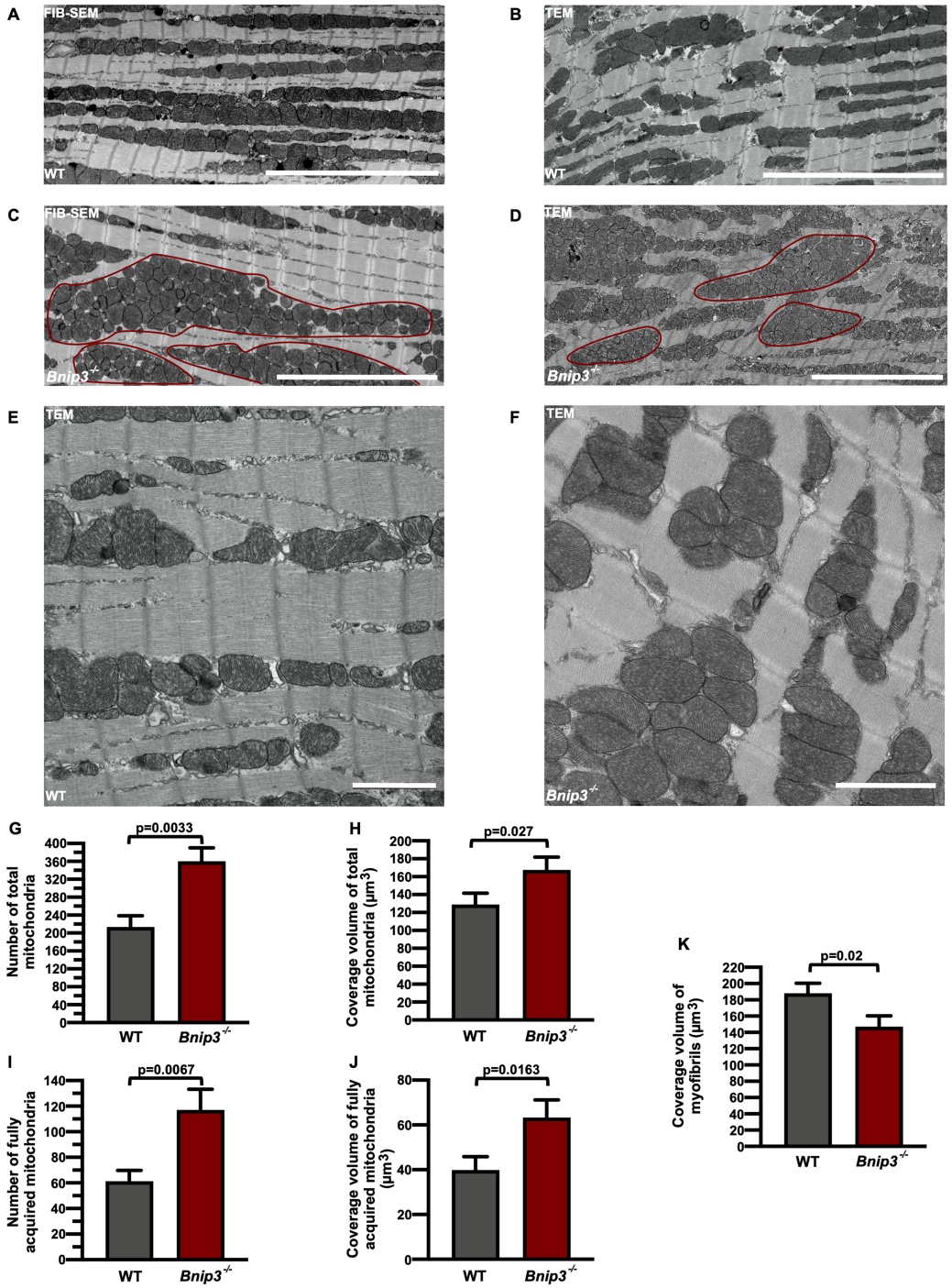

Figure 5 *Bnip3* deletion leads to alterations in mitochondrial number and dispersion. (*A*,*B*) representative section of a focused ion beam-scanning electron microscopy (FIB-SEM) stack (*A*) and a two-dimensional (2D) transmission electron microscopy (TEM) image (*B*) showing the arrangement and distribution of wild-type (WT) left ventricular (LV) mitochondria. Scale bar, 10 μm. (*C*,*D*) Representative section of a FIB-SEM stack (*C*) and a 2D TEM image (*D*) showing the arrangement, distribution and especially the cluster formation of mitochondria (red outline) in *Bnip3*$^{-/-}$ LV tissue. Scale bar, 10 μm. Refer to *Movie* S7 for animation. (*E*,*F*) Representative 2D electron micrographs of WT and *Bnip3*$^{-/-}$ LV tissue generated by TEM. Scale bar, 2 μm. (*G*) Average number of WT and *Bnip3*$^{-/-}$ total mitochondria. Data are the mean ± SD; *n* = 3 WT (4 FIB-SEM stacks) and three *Bnip3*$^{-/-}$ mice (3–4 FIB-SEM stacks). (*H*) Average coverage volume for WT and *Bnip3*$^{-/-}$ total mitochondria. Data are the mean ± SD; *n* = 3 WT (4 FIB-SEM stacks) and three *Bnip3*$^{-/-}$ mice (3–4 FIB-SEM stacks). (*I*) Average number of WT and *Bnip3*$^{-/-}$ mitochondria. Data are the mean ± SD; *n* = 3 WT (4 FIB-SEM stacks) and three *Bnip3*$^{-/-}$ mice (3–4 FIB-SEM stacks). (*J*) Average coverage volume of WT and *Bnip3*$^{-/-}$ mitochondria. Data are the mean ± SD; *n* = 3 WT (4 FIB-SEM stacks) and three mice (3–4 FIB-SEM stacks) *Bnip3*$^{-/-}$. (*K*) Average coverage volume of WT and *Bnip3*$^{-/-}$ myofibrils. Data are the mean ± SD; *n* = 3 WT (4 FIB-SEM stacks) and three *Bnip3*$^{-/-}$ mice (3–4 FIB-SEM stacks). Refer also to *Figure* S2.

DOI: 10.1002/jcsm.12742

mitochondria/μm^3; *Figure* 5I) was found, with a mean volume coverage of 63 μm^3 = 20% (*Figure* 5J). Regarding the number of completely acquired organelle bodies, these results suggested that the *Bnip3*$^{-/-}$ cardiomyocytes contained on average 1.9× more mitochondria than the WT cardiomyocytes (117 for *Bnip3*$^{-/-}$ vs. 61 for WT) with similar volume of the *Bnip3*$^{-/-}$ and WT cardiomyocytes (*Bnip3*$^{-/-}$: 2.0×10^4 $\mu m^3 \pm 0.5 \times 10^4$ μm^3, WT: 2.1×10^4 $\mu m^3 \pm 0.4 \times 10^{4-}$ μm^3, *Figure* S2A,C). This difference in organelle number corresponds to the outcome of mitochondrial isolation from whole mouse hearts. Here, it was found that on average, 1.52× more mitochondria could be isolated from the *Bnip3*$^{-/-}$ hearts than the WT counterparts (*Figure* S2D; $P < 0.0001$). Because we measured a significantly greater volume coverage by mitochondria in *Bnip3*$^{-/-}$ cardiomyocytes than in WT cardiomyocytes, we examined whether this increase was accompanied by a corresponding decrease in volume coverage by myofibrils (*Figure* 5K). Although the average myofibril volume coverage was significantly lower in the *Bnip3*$^{-/-}$ LV tissue samples (147 μm^3) than in the WT LV tissue samples (188 μm^3), a decrease in the myofibril protein actin could not be demonstrated statistically (*Figure* S2E). Hence, the decrease in the myofibril coverage area is due to a greater degree of myofibril compression in *Bnip3*$^{-/-}$ cardiomyocytes rather than attenuated myofibril biosynthesis.

Bnip3$^{-/-}$ *mitochondria are smaller and less complex than WT mitochondria*

Because approximately 25% more mitochondria occupied the same space in the analysed volume of *Bnip3*$^{-/-}$ LV tissue compared with the WT samples, the mitochondria were expected to be smaller in size, accordingly. To prove this assumption, we compared the volumes of 729 WT and 1285 *Bnip3*$^{-/-}$ fully acquired mitochondria in cardiac tissue samples. The mean individual mitochondrial volume did not appear to differ significantly (*Figure* 6A inset). However, cumulative frequency analyses showed considerable variations (*Figure* 6A). Therefore, we focused the volume distribution more precisely. *Bnip3*$^{-/-}$ cardiomyocytes showed a volume range from 0.2735 to 0.742 μm^3 for 50% of mitochondria and a mitochondrial volume maximum of 3.674 μm^3, whereas 50% of WT mitochondria ranged from a similar numerical baseline (0.214 μm^3) to 0.948 μm^3 (*Figure* 6B). Remarkably, the WT mitochondria showed a 38% greater maximum volume (5.062 μm^3) than the *Bnip3*$^{-/-}$ mitochondria (*Figure* 6B). Comparison of the distribution parameter in the population of either single samples or of the mice showed a significantly higher coefficient of variation in both cases for the WT group, which confirmed the more heterogeneous volume distribution under WT conditions (*Figure* 6C; samples $P < 0.0001$; mice $P = 0.0221$).

Because an altered fission/fusion cycle can lead to smaller mitochondria and increased number, we performed semi-quantitative western blot analysis of the fusion-related proteins OPA1 and OMA1 in *Bnip3*$^{-/-}$ and WT mouse heart homogenates. Whereas *Bnip3*$^{-/-}$ and WT mouse mice showed similar OPA1 levels (*Figure* S2F; $n = 3$ mice per group; $P = 0.7913$), the level of OMA1, which plays a key role in the stress-induced cleavage of OPA1 into a shorter, fusion-inactive form,[47] was higher in *Bnip3*$^{-/-}$ mouse hearts in comparison to WT mouse hearts (*Figure* S2G; $n = 3$ mice per group; $P = 0.0875$). This might indicate an increased inhibition of fusion in *Bnip3*$^{-/-}$ mice, thereby causing a shift of mitochondrial fission/fusion regulation in favour of fission. Future experiments are needed here.

Because the 3D mapping of mitochondria disclosed a high complexity of mitochondrial shape with round, elongated, flattened, and polymorphic entities (*Figure* 2D, *Movie* S2), we evaluated whether mitochondrial complexity significantly differed between the two genetically different mouse strains. Therefore, we used the 729 WT and 1285 *Bnip3*$^{-/-}$ mitochondria and calculated the MCI,[39] which describes the relationship between the mitochondrial surface area and volume without taking size values into consideration. Compared with the WT organelles, the *Bnip3*$^{-/-}$ mitochondria were on average 12% less complex (*Figure* 6D, inset; $P < 0.0001$). The MCI population dispersions were significantly different as determined by cumulative frequency distribution analysis (*Figure* 6D,E). Fifty per cent of the *Bnip3*$^{-/-}$ mitochondria displayed MCI values ranging from 4.156 to 5.931, whereas the MCI values of the WT mitochondria ranged from 4.236 to 6.791. The MCI population distributions differed considerably in the abundance of complex mitochondria (above the 90th percentile), with maxima of 25.42 (WT) and 21.27 (*Bnip3*$^{-/-}$). Comparison of the distribution between the WT and *Bnip3*$^{-/-}$ mitochondrial MCI yielded a similar coefficient of variation for samples and mice (*Figure* 6F; samples $P < 0.2875$; mice $P = 0.1595$).

To capture the shape complexity, we examined the form variability of the 729 WT and 1285 *Bnip3*$^{-/-}$ mitochondria. Therefore, we calculated the roundness (r), elongation (e), and flatness (f) values of each mitochondrion. The degree of each parameter is described by a range from 0–1. Mitochondria were classified as globular (r: 0–0.4; e: 0.5–1; f: 0–1), rod-shaped (r: 0.5–1; e: 0–0.4; f: 0.5–1), long-striped (r: 0.5–1; e: 0–0.4; f: 0–0.4), flattened (r: 0.5–1; e: 0.5–1; f: 0–0.4), and soft square-shaped (r: 0.5–1; e: 0.5–1; f: 0.5–1) (*Figure* 6G; *Figure* S3). In the *Bnip3*$^{-/-}$ group, more than 80% of the mitochondria were distributed along the three axes, being globular (17%), rod-shaped (20%) or soft square-shaped (47%). Sixteen per cent of mitochondria were limited along two of three axes, possessing a long-striped (6%) or flattened shape (10%) (*Figure* 6H). In contrast, there were 3.3 times more WT than *Bnip3*$^{-/-}$ mitochondria that were long-striped (16%) or flattened (36%). Seven per cent

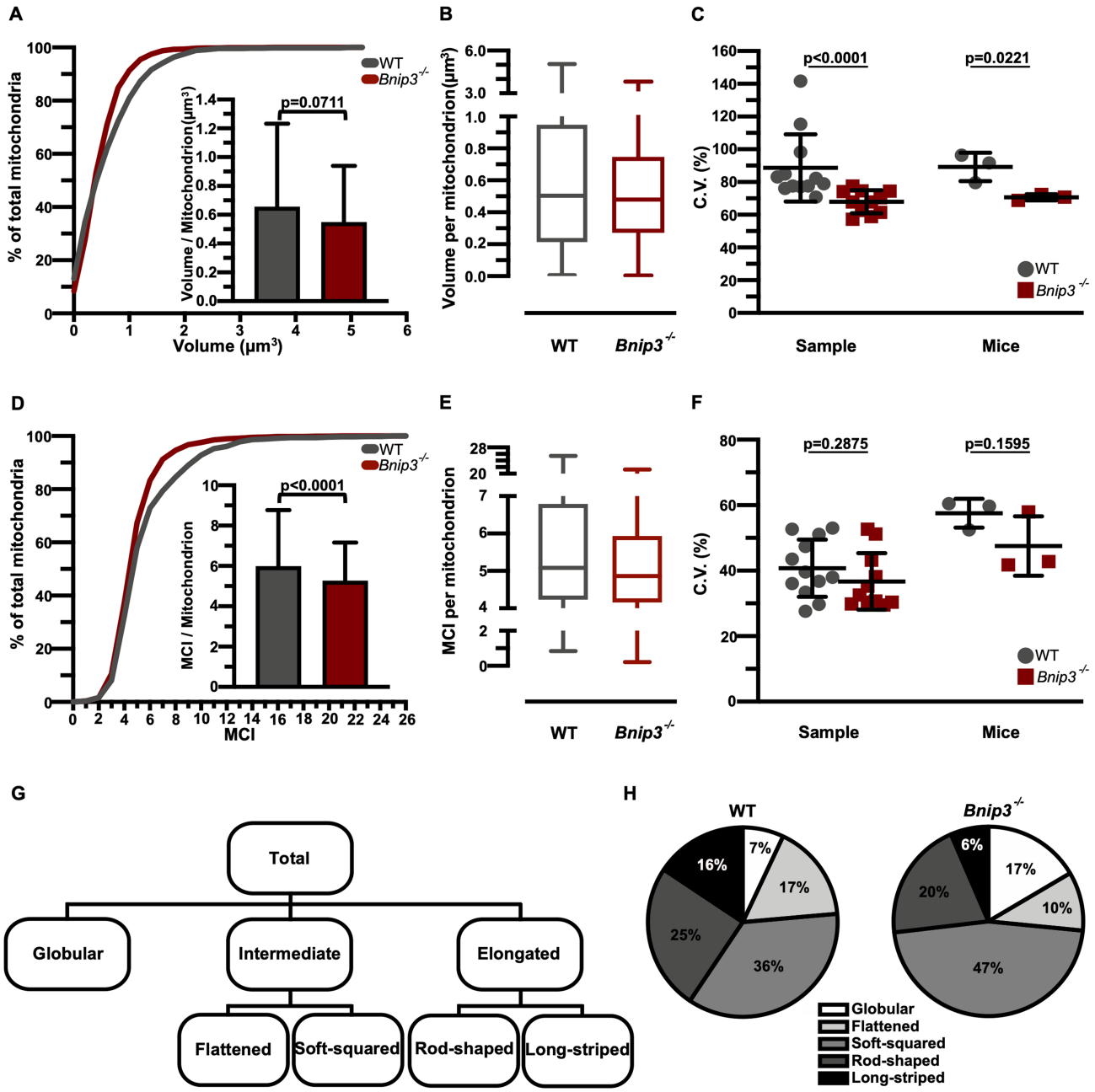

Figure 6 *Bnip3* $^{-/-}$ cardiac mitochondria are smaller and less complex than wild-type (WT) cardiac mitochondria. (*A*,*B*) Population distribution of individual mitochondrial volume in focused ion beam-scanning electron microscopy (FIB-SEM) stacks from WT (grey) and *Bnip3*$^{-/-}$ (red) mice. (*A*) Shown as cumulative frequency distribution, inset: mean ± SD (*n* = 729 in WT; *n* = 1285 in *Bnip3*$^{-/-}$, Mann–Whitney test). (*B*) Shown as box and whisker plots (min to max percentiles and median). (*C*) Coefficient of variation (CV) for mitochondrial volume in wild-type (WT) and *Bnip3*$^{-/-}$ mice. CV values are shown for mitochondria in FIB-SEM samples (*n* = 11–12) and in mice (*n* = 3). Data are shown as the mean ± SD. (*D*) Mitochondrial complexity index (MCI) in WT and *Bnip3*$^{-/-}$ mice shown as cumulative frequency distribution and average (inset). Mean ± SD (*n* = 729 in WT; *n* = 1285 in *Bnip3*$^{-/-}$, Mann–Whitney test). (*E*) MCI in WT and *Bnip3*$^{-/-}$ mice shown as box and whisker plots (min to max percentiles and median). (*F*) CV for MCI in WT and *Bnip3*$^{-/-}$ mice (*n* = 11–12 samples; *n* = 3 mice). Data are shown as the mean ± SD. (*G*) Assessment scheme of mitochondrial shape. Three-dimensional (3D) approaches enable the determination of a further spatial dimension and hence allow better alignment in shape groups. Roundness (r), elongation (e) and flatness (f) scores were used to classify mitochondria as globular (r: 0–0.4; e: 0.6–1; f: 0.6–1), rod-shaped (r: 0.6–1; e: 0–0.4; f: 0.5–1), long-striped (r: 0.8–1; e: 0–0.4; f: 0–0.4), flattened (r: 0.6–1; e: 0.5–1; f: 0–0.4) and soft square-shaped (r: 0.5–1; e: 0.5–1; f: 0.5–1). Refer also to *Figure* S3. (*H*) Proportions of the mitochondrial shape populations in WT (left panel) and *Bnip3*$^{-/-}$ (right panel) mice.

of WT mitochondria depicted a globular shape, 25% a rod shape and 36% a soft square shape (*Figure* 6H).

Collectively, *Bnip3*$^{-/-}$ cardiomyocytes had more mitochondria arranged in clusters than WT cardiomyocytes, at the expense of a decreased myofibril area. *Bnip3*$^{-/-}$ mitochondria, when compared with WT mitochondria, appeared more often with a lower volume and were less complex, while being almost globular, rod-shaped or soft square-shaped and less flattened in shape. These data indicate a physiological role of BNIP3 in the control of mitochondrial quantity and morphology.

Changes in Bnip3$^{-/-}$ *mitochondrial morphology and organization alter energy metabolism*

To understand the correlation between the size, shape and density distribution of mitochondria and energy metabolism, we mapped functional differences between WT and *Bnip3*$^{-/-}$ mitochondria by quantifying the oxygen consumption rate (OCR) using Seahorse® XF extracellular flux analyser technology (*Figure* 7A). *Bnip3*$^{-/-}$ mitochondria showed higher respiratory indices than WT mitochondria, as evidenced by significantly elevated oxygen consumption at baseline (*Figure* 7B). Compared with WT mitochondria, they also exhibited greater respiration activity after adenosine diphosphate injection (*Figure* 7C). Blockage of adenosine triphosphate (ATP) synthase with oligomycin resulted in a greater drop in the OCR in *Bnip3*$^{-/-}$ mitochondria than in WT mitochondria, reflecting greater ATP production in mitochondria in the genetically modified animals (*Figure* 7D). Remarkably, *Bnip3*$^{-/-}$ mitochondria also displayed greater proton leak. As proton leak represents protons that migrate into the mitochondrial matrix without producing ATP, BNIP3 ablation is attributed to a more incomplete coupling of substrate oxygen to ATP generation (*Figure* 7E). We conclude that the increased quantity and function associated with a distorted myofibril region in *Bnip3*$^{-/-}$ cardiomyocytes might play a compensatory role for contractility by increasing ATP levels. This was also supported by the echocardiographic observation that the LV function of *Bnip3*$^{-/-}$ animals was not impaired compared with that of WT animals, as judged by the similarity in the ejection fraction (55.5% vs. 51.68%), cardiac output (14.6 mL/min vs. 15.72 mL/min) and stroke volume (30.3 μL vs. 32.99 μL). *Bnip3*$^{-/-}$ mouse hearts even showed slightly increased fractional shortening (33.6% vs. 25.61%; *Figure* 7F).

Discussion

Although several studies on different cell systems have described a correlation between the morphology and function of mitochondria,[39,48,49] it remains challenging to identify clear links between cardiomyocyte mitochondrial ultrastructure and dysfunction in cardiac diseases. Notably, mitochondria of cardiomyocytes distinguish from non-cardiac mitochondria, for example, in that they are rather static than dynamic and immobile compared with mitochondria of fibroblasts, which are highly dynamic and motile, and mitochondria of neurons, which are dynamic and highly motile. Therefore, the findings from non-cardiac systems are not directly transferable to cardiac systems.[50] Our work aimed to shed light on the crucial question of whether a 2D EM analysis of the cardiomyocyte ultrastructure is sufficient to comprehensively describe the mitochondrial compartment and whether such planar imaging data are suited to correlate mitochondrial morphological data. To be able to judge acquired 2D EM data, we established a comparative 3D imaging system based on FIB-SEM nanotomography.

In the past, many widely recognized studies have used a variety of cell culture models to improve our understanding of the molecular and cellular basis of cardiac function and differentiation and to develop valuable therapeutic concepts. Hence, we first used FIB-SEM to investigate the ultrastructure of isolated cardiomyocytes. Only a few studies describe morphological differences between isolated cardiomyocytes either grown in 2D or 3D culture or remaining inside the 3D environment of cardiac tissue.[51] Most of these works dealt with differences in physiological parameters or in gene expression patterns.[51,52] Our first 3D analysis on the mitochondrial distribution pattern inside isolated cardiomyocytes demonstrated that the isolation process already altered the mitochondrial network distribution inside the cell. In contrast to cardiomyocytes *in situ*, most of the mitochondria inside the isolated cells were located at the cellular borders. This finding immediately underlined the importance of always taking structural post-isolation modifications into account and highlights that isolated cardiomyocytes are not the best-suited model for the characterization of the spatial distribution pattern of cardiomyocyte mitochondria. The differences in 3D over a 2D analysis for qualitative image interpretation holds true for parameters, including the mitochondrial number, dispersion space, size, and shape variety. The absence of any correlation or equivalent pattern of changes between the 2D and 3D data substantiated that apart from qualitative descriptions, 3D analysis was also indispensable for the accurate quantification of mitochondrial alterations. Moreover, the value of a 3D reconstruction was found in the numerous observations that one and the same mitochondrion is able to intersperse within the fibrillar network. In contrast to other studies,[53,54] these findings corroborate our former results showing that a general morphological discrimination of cardiac mitochondria between subtypes,[55] such as IFM or SSM is not meaningful.[43] Because most of these interfibrillar mitochondria located near the cell border crossed myofibril bundles in higher or lower cell areas and finally branched into

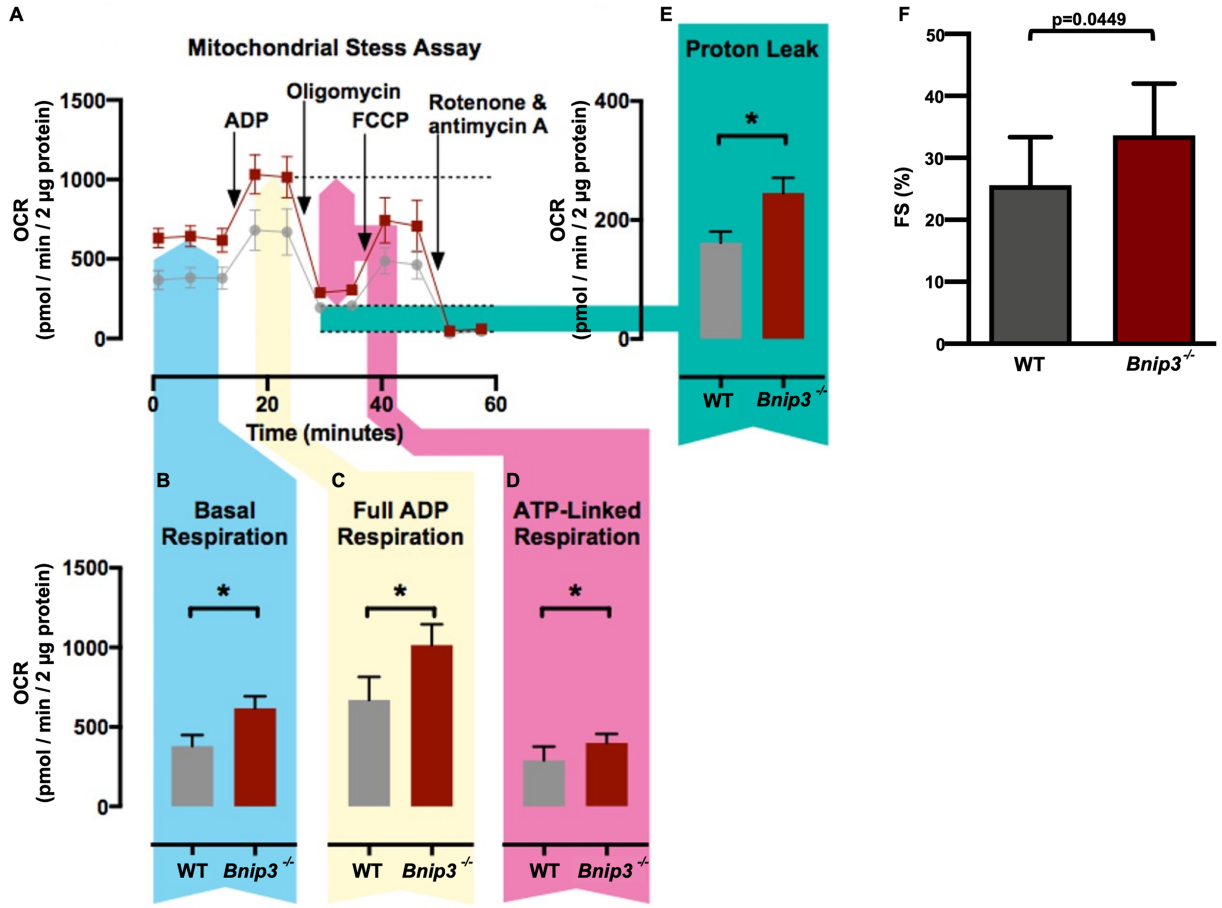

Figure 7 Changes in *Bnip3*$^{-/-}$ mitochondrial morphology and organization alter energy metabolism. (*A*–*E*) Respiration in isolated mitochondria from wild-type (WT, red) and *Bnip3*$^{-/-}$ mice (grey). Data are the mean ± SD (*n* = 5 mice). (*A*) Development of the oxygen consumption rate (OCR) after the addition of adenosine diphosphate (ADP) [adenosine triphosphate (ATP) synthesis initiation], oligomycin (respiratory chain complex V blocking), 4-(trifluoromethoxy) phenylhydrazone (FCCP; uncoupling of ATP synthesis from electron transport), rotenone and antimycin A (entire electron chain blocking through inhibition of Complexes I and III). (*B*) Basal respiration. (*C*) Full ADP respiration. (*D*) ATP-linked respiration. (*E*) Proton leakage. (*F*) Echocardiography of wild-type (WT) and *Bnip3*$^{-/-}$ mice showing fractional shortening (FS). Data are the mean ± SD (*n* = 5 mice per group).

the subsarcolemmal space, therefore, these mitochondria could be assigned to both subpopulations. Nevertheless, it can be assumed that mitochondria according to their *in situ* localization in different environments such as myofibrils or close to the sarcolemma, respectively, may depict different biochemical activities.

Crucial for an appropriate number and morphology of mitochondria is a dynamic balance between antagonistic forces of mitochondrial fusion and fission.[56] In contrast to confocal microscopy, EM represents the best suited microscopy technique for analysing ultrastructural changes in the course of membrane fusion and fission processes due to a sufficiently high resolution. Our results depict that 3D has the advantage to discriminate two individual only closely attached mitochondria from a mitochondrion being in the fusion or fission process but we are aware that we have to improve FIB-SEM technique for better resolution with a gain in uncovering membrane ultrastructures with focus on the cristae. In addition, our results confirmed that the lack of z-axis information does not allow precise definition of the actual morphological architecture of cardiomyocyte mitochondria with a high degree of complexity and spatial spread, underlining the need for 3D rendering.[57] In summary, a comparison of the 3D results with the corresponding 2D data revealed that a plain 2D analysis yielded biased data regarding mitochondrial quantity and morphology and therefore was unable to accurately reflect cardiac mitochondrial peculiarities *in situ*.

The value of the 3D analysis was verified by evaluation of the morphological, quantitative and distributional differences in cardiomyocyte mitochondria lacking BNIP3. BNIP3 is supposed to constitute a key factor in the induction of mitophagy described in various cell types associated with cell-protective effects as well as with cell death.[58–64] BNIP3's promitophagic activity in cardiomyocytes *in vivo* is linked to pathologies and has been shown to be maladaptive.[26,65,66] Despite the increased appearance of mitochondria in cardiomyocytes

lacking *Bnip3*, no evident damaged or dysfunctional mitochondria could be observed, indicating that mitophagy was not substantially impaired. But the observation of a greater number of mitochondria, which were smaller and less complex in *Bnip3*$^{-/-}$ cardiomyocytes suggests a role of BNIP3 in the fusion/fission cycle. At first glance, this cycle does not appear to be a relevant process for myocardial biology, as cardiomyocyte mitochondria are regarded to be rather static due to the dense myofilament arrangement.[67] Studies with the combined abrogation of fission and fusion proteins or a disturbed balance indicated the relevance of the fusion/fission cycle to cardiac health, as its perturbation was detrimental to the heart. This is also observed in, for example, dilated cardiomyopathy, heart failure, and LV hypertrophy.[67–70] In these cases, mitochondria are accumulated, shortened, and damaged. In addition, as in our observations, displacement of sarcomeres by superabundant centrally located mitochondria was noted. These alterations were also apparent in the cardiac biopsy of a human patient suffering from myocarditis (*Figure* S4, *Movie* S8). In preclinical studies, myocarditis has also been linked to an imbalance in the fusion/fission cycle.[71,72] All of these features, except damaged mitochondria, were equally observed in cardiomyocytes lacking BNIP3 under natural conditions. The phenomenon of an increased number of smaller mitochondria without obvious ultrastructural damage in cardiomyocytes lacking BNIP3 was likewise observed in mouse hearts overexpressing the fission protein DRP1.[6] Taking into consideration that both DRP1 overexpression and BNIP3 deletion led to advanced fission, a regulatory involvement of BNIP3 in fusion processes is tempting to speculate. Regarding that, BNIP3 interacts with the fusion-related protein OPA1 in HeLa cells.[73] BNIP3 may regulate OPA1 in an activating manner in cardiomyocytes. This is supported by the finding that the level of OMA1, which plays a key role in cleavage of OPA 1 into a fusion-inactive form, is elevated in *Bnip3*$^{-/-}$ mouse hearts, which might result in an increased inhibition of fusion, thereby causing a shift in favour of fission.

In terms of bioenergetics, our data show that the loss of BNIP3 also affects the cardiomyocyte energy metabolism, with an increase in dioxygen consumption and ATP generation. This effect was associated with a slight increase in fractional shortening. The increase in respiration reflects the fitness of cardiomyocyte mitochondria in *Bnip3*$^{-/-}$ mice and could point to a compensatory mechanism to rescue cardiomyocyte contraction. As a mode of action, we hypothesize that the apparent clustering of more rounded mitochondria may result in greater interconnectivity.[74] A similar phenomenon was also observed in diabetes, where clusters of mitochondria showed increased respiration.[75] These morphological and biochemical data suggest a physiological function of BNIP3 as a primary driver of the fusion/fission cycle regulating the homeostasis of cardiac bioenergetics.

In conclusion, this work demonstrates and underlines the need for 3D imaging approaches when the cardiomyocyte mitochondrial network is the target of a qualitative or quantitative microscopic analysis. Our data clearly prove that 2D image materials are prone to misinterpretation and that the superior 3D approach allows the accurate interpretation of mitochondrial alterations, providing a suggestion of the role of mitochondrial regulatory proteins such as BNIP3.

Funding

J. H.-W. was funded by Juergen Manchot Stiftung; S. S. was supported by the German Research Foundation (UMEA Junior Clinician Scientist); P. L. (LU 2139/2-1) and U. B. H.-C (HE 6317/2-1) were funded by the German Research Foundation; and T. R. was funded by Else-Kroener-Fresenius-Stiftung (2014_A216) and the German Research Foundation (RA 969/12-1).

Author contributions

Conceptualization was carried out by Ulrike B. Hendgen-Cotta; methodology was created by Elke Winterhager, Mike Hasenberg, and Ulrike B. Hendgen-Cotta; supervision was provided by Tienush Rassaf, Mike Hasenberg, and Ulrike B. Hendgen-Cotta; investigation was performed by Jacqueline Heinen-Weiler, Anna-Lena Beerlage, Stephan Settelmeier, and Hannah Doepper; human tissue acquisition and clinical information was carried out by Peter Luedike; data analysis and interpretation was performed by Jacqueline Heinen-Weiler, Anna-Lena Beerlage, Stephan Settelmeier, Martin Heisler, Elke Winterhager, and Ulrike B. Hendgen-Cotta; statistical analysis was performed by Jacqueline Heinen-Weiler, Martin Heisler, Bernd Walkenfort, Ulrike B. Hendgen-Cotta; writing of the original draft of the manuscript was carried out by Elke Winterhager, Mike Hasenberg, Ulrike B. Hendgen-Cotta; all authors performed critical revision of the manuscript.

Acknowledgements

The authors certify that they comply with the ethical guidelines for authorship and publishing in the *Journal of Cachexia, Sarcopenia and Muscle*.[76]

We gratefully acknowledge the technical assistance of Pia Stock (Department of Cardiology and Vascular Medicine). In addition, we would like to thank the Imaging Center Essen (IMCES) for unlimited technical support, Sylvia Voortmann for technical assistance and Dr Holger Jastrow for his scientific input. Further, we thank Dr Gerald Dorn II, MD, for the gift of the *Bnip3*$^{-/-}$ mice.

Online supplementary material

Additional supporting information may be found online in the Supporting Information section at the end of the article.

Movie S1. 3D reconstruction of the mitochondrial network inside an isolated cardiomyocyte. Related to Figure 1A-C. The movie first shows the virtual flight through an isolated mousecardiomyocyte. The mitochondrial areas are visible in dark grey whereas myofibrils can be identified from their light grey appearance. All individual images represent x-y single plane pictures of a FIB-SEM analysis of which the resulting z stack was composed of 705 images at a z-distance of 100 nm. The total dimensions of the analysed volume equaled 77.35 x 49.96 x 70.5 μm (isolated cardiomyocyte size 37.39 x 20.31 μm (xy-axis) and 79.27 x 18.11 μm (yzaxis)). In the second part of the movie, the result of an ultrastructural segmentation of that cardiomyocyte is developed as 3D model. For that, the outer cell membrane is displayed in blue, myofibrils are highlighted in yellow, nuclei in green and mitochondria in red. Please note that the myofibril compartment was rendered transparent at the end of the movie to clearly depict the course of the mitochondrial network in a 360° rotation. Scale bar 15 μm.

Movie S2. 3D reconstruction of the mitochondrial network inside mouse cardiac tissue. Related to Figure 1D. The movie first shows the virtual flight through a mouse cardiac biopsy sample. The mitochondrial areas are visible in dark grey whereas myofibrils can be identified from their light grey appearance. All individual images represent x-y single plane pictures of a FIB/SEM analysis of which the resulting z stack was composed of 21 images at a z-distance of 150 nm. The total dimensions of the analysed volume equaled 10 x10 x 3.15 μm. In the second part of the movie, the result of an ultrastructural tissue segmentation is shown as 3D model. In the beginning of the rotation just the surface view of the volume is visualized where the contours of the mitochondria are depicted in dark blue and the interspersed myofibrils in light blue. Subsequently, the myofibril compartment is rendered transparent so that the inner part of the volume is revelled. Now, all mitochondria are shown as 3D objects in individual colours and lipid droplets in black. After a 360 ° rotation, all partially acquired mitochondrial bodies are removed so that the shape variety of the individual mitochondria of round, elongated and polymorph can be easily assessed. Scale bar 1.6 μm.

Movie S3. 3D Reconstruction of a complex mitochondrion inside mouse cardiac tissue is a prerequisite for proper quantification. Related to Figure 1E, F. The movie first shows the virtual flight through a mouse cardiac biopsy sample. The mitochondrial areas are visible in dark grey whereas myofibrils can be identified from their light grey appearance. All individual images represent x-y single plane pictures of a FIB-SEM analysis of which the resulting z stack was composed of 100 images at a z-distance of 20 nm. The total dimensions of the analysed volume equaled 6.45 x 3.78 x 2 μm (x/y/z-axis). In the second part of the movie, the result of an individual mitochondrial segmentation is shown as very large 3D model in turquoise (mitochondrion size up to 6 μm). Please note the appearance of this single but branched mitochondrion as several organelles at different planes of the z-stack. Scale bar 1.2 μm.

Movie S4. 3D Reconstruction of a complex mitochondrion inside mouse cardiac tissue is a prerequisite for proper classification. Related to Figure 1G. The movie shows the virtual flight through a mouse cardiac biopsy sample during which the result of an individual mitochondrial segmentation is shown as 3D model in turquoise. The mitochondrial areas are visible in dark grey whereas myofibrils can be identified from their light grey appearance. All individual images represent x-y single plane pictures of a FIB-SEM analysis of which the resulting z stack was composed of 48 images at a z-distance of 30 nm. The total dimensions of the analysed volume equaled 3.24 x 4.9 x 1.44 μm (x/y/z-axis). Please note the appearance of this single but branched mitochondrion as several organelles of the subsarcolemmal (SSM) or interfibrillar (IFM) type at different planes of the z-stack.

Movie S5. 3D Reconstruction of a single mitochondrion interspersing myofibrils. Related to Figure 1H. The movie shows the result of an ultrastructural segmentation of a mouse cardiac biopsy sample as 3D model. The single mitochondrion is visualized in green whereas the myofibrillar compartment which gets interspersed by the mitochondrion is highlighted in yellow. The underlying 3D model is a part of a FIB-SEM analysis which was performed on a sample volume of 4.51 x 6.69 x 3.57 μm generating Y individual single plane images at a voxel size of 3 x 3 x 30 nm. Scale bar 1 μm.

Movie S6. 3D analysis of cardiac mitochondrial fission process. Related to Figure 1 J, K. The movie shows the virtual flight through a mouse cardiac biopsy sample at the border zone during which ongoing fission process is visible. Also, a 3D model of both involved mitochondria is visible in turquoise coloured. The mitochondrial areas are visible in dark grey whereas myofibrils can be identified from their light grey appearance. All individual images represent x-y single plane pictures of a FIB-SEM analysis of which the resulting z stack was composed of 21 images at a z-distance of 20 nm. The total dimensions of the analysed volume equaled 3.06 x 2.08 x 0.42 μm (x/y/z-axis) (x/y/z-axis). Scale bar 1 μm.

Movie S7. 3D analysis of the mitochondrial network inside cardiac tissue of *Bnip3*$^{-/-}$ mice. Related to Figure 5C,D. The movie shows the virtual flight through a left ventricular biopsy sample of *Bnip3*$^{-/-}$ mice during which the contours of the segmented mitochondria are highlighted in red. The mitochondrial areas are visible in dark grey whereas myofibrils can be identified from their light grey appearance.

All individual images represent x-y single plane pictures of a FIB-SEM analysis of which the resulting z stack was composed of 21 images at a z-distance of 150 nm. The total dimensions of the analysed volume equaled 26.09 × 18.56 x 3.15 μm (x/y/z-axis). Please note the obviously altered arrangement, distribution and especially the cluster formation of the mitochondria compared to the wildtype situation. Scale bar 8.4 μm.

Movie S8. 3D Reconstruction of damaged mitochondria inside a human tissue biopsy of a myocarditis patient. Related to Supplemental Figure 4A, B. The movie first shows the virtual flight through a human cardiac biopsy sample of a patient suffering from myocarditis. The mitochondrial areas are visible in dark grey whereas myofibrils can be identified from their light grey appearance. All individual images represent x-y single plane pictures of a FIB-SEM analysis of which the resulting z stack was composed of 100 images at a z-distance of 20 nm. The total dimensions of the analysed volume equaled 4.64 x 6.21 x 2 μm. In the second part of the movie, the result of a mitochondrial segmentation is shown for which just mitochondria with an obvious damage of their ultrastructure were included. The 3D models of these mitochondria with affected ultrastructure are shown in individual colours. Please also note other indications of myocarditis, such as cluster formation of mitochondria with relatively small size and myofibril distortion. Scale bar 1.22 μm.

Figure S1. Quantitative 2D analyses does not reflect 3D facts. Related to Figure 3. (A) Individual deviation (%) of mitochondrial number in 2D (top section: upper panel; bottom section: lower panel) from mitochondrial number obtained from 3D reconstructions. (B) Individual deviation (%) of mitochondrial coverage areas (top section: upper panel; bottom section: lower panel) from mitochondrial volumes. (C) Cumulative frequency distribution of individual mitochondrial size in 3D and 2D. In 3D the size is considered as mitochondrial volume in 3D reconstructions (green). For 2D the size is considered as mitochondrial area in bottom section (grey). To enable comparisons despite unequal dimension number, roots of absolute values were extracted. (D) Representative histograms of individual mitochondrial size. Mitochondrial area frequency in the bottom section of four FIB-SEM stack was plotted in the upper panel (grey) and corresponding volume frequency in the 3D reconstruction in the lower panel (green). The curve shape describing parameters skewness and kurtosis are indicated. (E) Cumulative frequency distribution of individual mitochondrial shape parameter in 3D and 2D. In 3D, the shape is considered as mitochondrial surface area (green). For 2D, the shape is considered as mitochondrial perimeter in top sections (grey). To enable comparisons despite unequal dimension number, roots of absolute values were extracted. (F) Representative histograms of individual mitochondrial shape. Mitochondrial perimeter frequency in the bottom section of four FIB-SEM stack was plotted in the upper panel (grey) and corresponding surface area frequency in the 3D reconstruction in the lower panel (green). The curve shape describing parameters skewness and kurtosis are indicated. (12 FIB-SEM stacks, n = 3 wild-type mice).

Supplementary Figure S2. *Bnip3* deletion leads to mitochondrial protein changes. (A, B) Representative fluorescence images of isolated mouse cardiomyocytes from wild-type (WT) (A) and *Bnip3*$^{-/-}$ mice (B) (n = 3 mice each group; n = 6 cardiomyocytes each mouse). Cardiomyocytes were acquired in z-stacks, mitochondria (red), actin (green) and nuclei (blue). Scale bar, 50 μm. (C) Average volumes of isolated cardiomyocytes from WT (grey) and *Bnip3*$^{-/-}$ mice (red) (n = 3 mice each group; n = 6 cardiomyocytes each mouse). (D) Relative mitochondrial amount from WT and *Bnip3*$^{-/-}$ mouse hearts. (n = 8 mice each group). (E) Average of actin expression from WT and *Bnip3*$^{-/-}$ mouse hearts. (n = 3 each group). (F) Relative OMA1 expression from WT and *Bnip3*$^{-/-}$ mouse hearts (n = 3 each group). (G) Relative OPA1 expression from WT and *Bnip3*$^{-/-}$ mouse hearts (n = 3 each group). Data are mean ± SD.

Supplementary Figure S3. Mitochondrial shape classification. Related to Figure 6. Overview of shape groups with representative corresponding ellipsoids and 3D models from either xy-, xz- and yx-view. Polymorphic mitochondria are not represented in globular group.

Supplementary Figure S4. Imaging of human myocarditis. (A-D) 2D electron micrographs of heart tissue in human myocarditis (n = 1). TEM overview (A) and closeup image (B) of a longitudinal orientated cardiomyocyte depicting cluster formation (red) and damaged mitochondria (cyan) as well as distorted myofibrils (yellow). See also Supporting Information Movie S8

Supplementary Listing S1. Mitochondrial classification algorithm. Custom script to align mitochondria into shape groups based on Python coding language. Data are extracted from a coma separated value (.csv) file that listed the shape parameters of each unique mitochondrion in a separate row. Parameter ranges enter the algorithm via the dictionary object that refers to 'limits'.

Conflict of interest

Jacqueline Heinen-Weiler, Mike Hasenberg, Martin Heisler, Stephan Settelmeier, Anna-Lena Beerlage, Hannah Doepper, Bernd Walkenfort, Andrea Odersky, Peter Luedike, Elke Winterhager, Tienush Rassaf, Ulrike B. Hendgen-Cotta declare that they have no conflict of interest.

Data availability statement

Image stacks and model files are available from the authors upon request.

References

1. Bonora M, Wieckowski MR, Sinclair DA, Kroemer G, Pinton P, Galluzzi L. Targeting mitochondria for cardiovascular disorders: therapeutic potential and obstacles. *Nat Rev Cardiol* 2019;**16**:33–55.
2. Murphy E, Ardehali H, Balaban RS, DiLisa F, Dorn GW 2nd, Kitsis RN, et al. Mitochondrial function, biology, and role in disease: a scientific statement from the American Heart Association. *Circ Res* 2016;**118**: 1960–1991.
3. Tian R, Colucci WS, Arany Z, Bachschmid MM, Ballinger SW, Boudina S, et al. Unlocking the secrets of mitochondria in the cardiovascular system: path to a cure in heart failure—a report from the 2018 National Heart, Lung, and Blood Institute Workshop. *Circulation* 2019;**140**: 1205–1216.
4. Hendgen-Cotta UB, Giorgio V, Hool L. Mitochondria at the crossroads of survival and demise. *Oxid Med Cell Longev* 2019;**2019**:2608187.
5. Song M, Dorn GW 2nd. Mitoconfusion: noncanonical functioning of dynamism factors in static mitochondria of the heart. *Cell Metab* 2015;**21**:195–205.
6. Song M, Franco A, Fleischer J, Zhang L, Dorn GW 2nd. Abrogating mitochondrial dynamics in mouse hearts accelerates mitochondrial senescence. *Cell Metab* 2017;**26**:872–883, e5.
7. Brown DA, Perry JB, Allen ME, Sabbah HN, Stauffer BL, Shaikh SR, et al. Expert consensus document: mitochondrial function as a therapeutic target in heart failure. *Nat Rev Cardiol* 2017;**14**:238–250.
8. Treskatsch S, Shakibaei M, Feldheiser A, Shaqura M, Dehe L, Roepke TK, et al. Ultrastructural changes associated with myocardial apoptosis, in failing rat hearts induced by volume overload. *Int J Cardiol* 2015;**197**:327–332.
9. Takemura G, Onoue K, Kashimura T, Kanamori H, Okada H, Tsujimoto A, et al. Electron microscopic findings are an important aid for diagnosing mitochondrial cardiomyopathy with mitochondrial DNA mutation 3243A>G. *Circ Heart Fail* 2016;**9**:e003283.
10. Daghistani HM, Rajab BS, Kitmitto A. Three-dimensional electron microscopy techniques for unravelling mitochondrial dysfunction in heart failure and identification of new pharmacological targets. *Br J Pharmacol* 2019;**176**:4340–4359.
11. Sabbah HN. Targeting the mitochondria in heart failure: a translational perspective. *JACC Basic Transl Sci* 2020;**5**:88–106.
12. Garnham JO, Roberts LD, Caspi T, Al-Owais MM, Bullock M, Swoboda PB, et al. Divergent skeletal muscle mitochondrial phenotype between male and female patients with chronic heart failure. *J Cachexia Sarcopenia Muscle* 2020;**11**:79–88.
13. Hughes MC, Ramos SV, Turnbull PC, Rebalka IA, Cao A, Monaco CMF, et al. Early myopathy in Duchenne muscular dystrophy is associated with elevated mitochondrial H_2O_2 emission during impaired oxidative phosphorylation. *J Cachexia Sarcopenia Muscle* 2019;**10**: 643–661.
14. Walter MC, Reilich P. Recent developments in Duchenne muscular dystrophy: facts and numbers. *J Cachexia Sarcopenia Muscle* 2017;**8**:681–685.
15. McNally EM, Kaltman JR, Benson DW, Canter CE, Cripe LH, Duan D, et al. Contemporary cardiac issues in Duchenne muscular dystrophy. Working Group of the National Heart, Lung, and Blood Institute in collaboration with Parent Project Muscular Dystrophy. *Circulation* 2015;**131**:1590–1598.
16. Hughes MC, Ramos SV, Turnbull PC, Edgett BA, Huber JS, Polidovitch N, et al. Impairments in left ventricular mitochondrial bioenergetics precede overt cardiac dysfunction and remodelling in Duchenne muscular dystrophy. *J Physiol* 2020;**598**: 1377–1392.
17. Knowlton AA, Liu TT. Mitochondrial dynamics and heart failure. *Compr Physiol* 2015;**6**:507–526.
18. Liesa M, Shirihai OS. Mitochondrial dynamics in the regulation of nutrient utilization and energy expenditure. *Cell Metab* 2013;**17**:491–506.
19. Hoppel CL, Tandler B, Fujioka H, Riva A. Dynamic organization of mitochondria in human heart and in myocardial disease. *Int J Biochem Cell B* 2009;**41**:1949–1956.
20. Riva A, Faa G, Loffredo F, Piludu M, Riva FT. An improved OsO_4 maceration method for the visualization of internal structures and surfaces in human bioptic specimens by high-resolution scanning electron microscopy. *Scanning Microsc* 1999;**13**:111–122.
21. Riva A, Tandler B, Lesnefsky EJ, Conti G, Loffredo F, Vazquez E, et al. Structure of cristae in cardiac mitochondria of aged rat. *Mech of Age Develop* 2006;**127**: 917–921.
22. Xu CS, Hayworth KJ, Lu Z, Grob P, Hassan AM, Garcia-Cerdan JG, et al. Enhanced FIB-SEM systems for large-volume 3D imaging. *Elife* 2017;**6**:e25916.
23. Kubli DA, Quinsay MM, Huang C, Lee Y, Gustafsson AB. Bnip3 functions as a mitochondrial sensor of oxidative stress during myocardial ischemia/reperfusion. *Am J Physiol Heart Circ Physiol* 2008;**295**: H2025–H2031.
24. Hamacher-Brady A, Brady NR, Logue SE, Sayen MR, Jinno M, Kirshenbaum LA, et al. Response to myocardial ischemia/reperfusion injury involves Bnip3 and autophagy. *Cell Death Differ* 2007;**14**:146–157.
25. Mehrabani S, Bagherniya M, Askari G, Read MI, Sahebkar A. The effect of fasting or calorie restriction on mitophagy induction: a literature review. *J Cachexia Sarcopenia Muscle* 2020;**11**:1447–1458.
26. Diwan A, Krenz M, Syed FM, Wansapura J, Ren X, Koesters AG, et al. Inhibition of ischemic cardiomyocyte apoptosis through targeted ablation of Bnip3 restrains postinfarction remodeling in mice. *J Clin Invest* 2007;**117**:2825–2833.
27. Bravo-San Pedro JM, Kroemer G, Galluzzi L. Autophagy and mitophagy in cardiovascular disease. *Circ Res* 2017;**120**:1812–1824.
28. Du Q, Zhu B, Zhai Q, Yu B. Sirt3 attenuates doxorubicin-induced cardiac hypertrophy and mitochondrial dysfunction via suppression of Bnip3. *Am J Transl Res* 2017;**9**:3360–3373.
29. Li E, Li X, Huang J, Xu C, Liang Q, Ren K, et al. BMAL1 regulates mitochondrial fission and mitophagy through mitochondrial protein BNIP3 and is critical in the development of dilated cardiomyopathy. *Protein Cell* 2020;**11**:661–679.
30. Seligman A, Wasserkrug H, Hanker JA. A new staining method (OTO) for enhancing contrast of lipid-containing membranes and droplets in osmium tetroxide-fixed tissue with osmiophilic thiocarbohydrazide (TCH). *J Cell Biol* 1966;**30**:424–432.
31. Zhang Q, Duplany A, Moncollin V, Mouradian S, Goillot E, Mazelin L, et al. Lack of muscle mTOR kinase activity causes early onset myopathy and compromises whole-body homeostasis. *J Cachexia Sarcopenia Muscle* 2019;**10**:35–53.
32. Schindelin J, Arganda-Carreras I, Frise E, Kaynig V, Longair M, Pietzsch T, et al. Fiji: an open-source platform for biological-image analysis. *Nat Methods* 2012;**9**: 676–682.
33. Hendgen-Cotta UB, Esfeld S, Rudi K, Miinalainen I, Klare JP, Rassaf T. Cytosolic BNIP3 dimer interacts with mitochondrial BAX forming heterodimers in the mitochondrial outer membrane under basal conditions. *Int J Mol Sci* 2017;**18**:687.
34. Abreu P, Kowaltowski AJ. Satellite cell self-renewal in endurance exercise is mediated by inhibition of mitochondrial oxygen consumption. *J Cachexia Sarcopenia Muscle* 2020;**11**:1661–1676.
35. Rammos C, Hendgen-Cotta UB, Totzeck M, Pohl J, Ludike P, Flogel U, et al. Impact of dietary nitrate on age-related diastolic dysfunction. *Eur J Heart Fail* 2016;**18**:599–610.
36. Tsuda M, Fukushima A, Matsumoto J, Takada S, Kakutani N, Nambu H, et al. Protein acetylation in skeletal muscle mitochondria is involved in impaired fatty acid oxidation and exercise intolerance in heart failure. *J Cachexia Sarcopenia Muscle* 2018;**9**:844–859.
37. Lindsey ML, Kassiri Z, Virag JAI, de Castro Brás LE, Scherrer-Crosbie M. Guidelines for measuring cardiac physiology in mice. *Am J Physiol Heart Circ Physiol* 2018;**314**: H733–H752.
38. Bauer M, Cheng S, Jain M, Ngoy S, Theodoropoulos C, Trujillo A, et al. Echocardiographic speckle-tracking based strain imaging for rapid cardiovascular phenotyping in mice. *Circ Res* 2011;**108**: 908–916.
39. Vincent AE, White K, Davey T, Philips J, Ogden RT, Lawless C, et al. Quantitative 3D mapping of the human skeletal muscle

mitochondrial network. *Cell Rep* 2019;**27**:321.
40. Koopman WJH, Visch H-J, Verkaart S, van den Heuvel LWPJ, Smeitink JAM, Willems PHGM. Mitochondrial network complexity and pathological decrease in complex I activity are tightly correlated in isolated human complex I deficiency. *Am J Physiol Cell Physiol* 2005;**289**:C881–C890.
41. Cain MK, Zhang Z, Yuan KH. Univariate and multivariate skewness and kurtosis for measuring nonnormality: prevalence, influence and estimation. *Behav Res Methods* 2017;**49** :1716–1735.
42. Deerinck TJ, Bushong E, Thor A, Ellisman MH. NCMIR methods for 3D EM: A new protocol for preparation of biological specimens for serial block-face SEM. *Microscopy* 2010;**6**.
43. Hendgen-Cotta UB, Esfeld S, Jastrow H, Totzeck M, Altschmied J, Goy C, et al. Mouse cardiac mitochondria do not separate in subsarcolemmal and interfibrillar subpopulations. *Mitochondrion* 2018;**38**:1–5.
44. Rosca MG, Tandler B, Hoppel CL. Mitochondria in cardiac hypertrophy and heart failure. *J Mol Cell Cardiol* 2013;**55**:31–41.
45. Rosca MG, Hoppel CL. Mitochondrial dysfunction in heart failure. *Heart Fail Rev* 2013;**18**:607–622.
46. Dorn GW 2nd. Mitochondrial dynamism and heart disease: changing shape and shaping change. *EMBO Mol Med* 2015;**7**:865–877.
47. Ehses S, Raschke I, Mancuso G, Bernacchia A, Geimer S, Tondera D, et al. Regulation of OPA1 processing and mitochondrial fusion by m-AAA protease isoenzymes and OMA1. *J Cell Biol* 2009;**28**:1023–1036.
48. Gomes LC, Di Benedetto G, Scorrano L. During autophagy mitochondria elongate, are spared from degradation and sustain cell viability. *Nat Cell Biol* 2011;**13**:589–598.
49. Trushina E, Nemutlu E, Zhang S, Christensen T, Camp J, Mesa J, et al. Defects in mitochondrial dynamics and metabolomic signatures of evolving energetic stress in mouse models of familial Alzheimer's disease. *PLoS One* 2012;**7**: e32737.
50. Dorn GW 2nd. Cardiac-specific research platforms engender novel insights into mitochondrial dynamism. *Curr Opin Physiol* 2018;**3**:110–115.
51. Soares CP, Midlej V, de Oliveira MEW, Benchimol M, Costa ML, Mermelstein C. 2D and 3D-organized cardiac cells shows differences in cellular morphology, adhesion junctions, presence of myofibrils and protein expression. *PLoS One* 2012;**7**: e38147.
52. Akins RE Jr, Rockwood D, Robinson KG, Sandusky D, Rabolt J, Pizarro C. Three-dimensional culture alters primary cardiac cell phenotype. *Tissue Eng Part A* 2010; **16**:629–641.
53. Boengler K, Stahlhofen S, van de Sand A, Gres P, Ruiz-Meana M, Garcia-Dorado D, et al. Presence of connexin 43 in subsarcolemmal, but not in interfibrillar cardiomyocyte mitochondria. *Basic Res Cardiol* 2009;**104**:141–147.
54. Koncsos G, Varga ZV, Baranyai T, Ferdinandy P, Schulz R, Giricz Z, et al. Nagarse treatment of cardiac subsarcolemmal and interfibrillar mitochondria leads to artefacts in mitochondrial protein quantification. *J Pharmacol Toxicol Methods* 2018;**91**:50–58.
55. Boengler K, Kosiol M, Mayr M, Schulz R, Rohrbach S. Mitochondria and ageing: role in heart, skeletal muscle and adipose tissue. *J Cachexia Sarcopenia Muscle* 2017;**8**: 349–369.
56. Chen Y, Dorn GW 2nd. PINK1-phosphorylated mitofusin 2 is a Parkin receptor for culling damaged mitochondria. *Science* 2013;**340**:471–475.
57. Kalkhoran SB, Hall AR, White IJ, Cooper J, Fan Q, Ong S-B, et al. Assessing the effects of mitofusin 2 deficiency in the adult heart using 3D electron tomography. *Physiol Rep* 2017;**5**:e13437.
58. Daido S, Kanzawa T, Yamamoto A, Takeuchi H, Kondo Y, Kondo S. Pivotal role of the cell death factor BNIP3 in ceramide-induced autophagic cell death in malignant glioma cells. *Cancer Res* 2004;**64**:4286–4293.
59. Kanzawa T, Zhang L, Xiao L, Germano IM, Kondo Y, Kondo S. Arsenic trioxide induces autophagic cell death in malignant glioma cells by upregulation of mitochondrial cell death protein BNIP3. *Oncogene* 2005;**24**:980–991.
60. Gao A, Jiang J, Xie F, Chen L. Bnip3 in mitophagy: novel insights and potential therapeutic target for diseases of secondary mitochondrial dysfunction. *Clin Chim Acta* 2020;**506**:72–83.
61. Mammucari C, Milan G, Romanello V, Masiero E, Rudolf R, Del Piccolo P, et al. FoxO3 controls autophagy in skeletal muscle in vivo. *Cell Metab* 2007;**6**:458–471.
62. Tracy K, Dibling BC, Spike BT, Knabb JR, Schumacker P, Macleod KF. BNIP3 is an RB/E2F target gene required for hypoxia-induced autophagy. *Mol Cell Biol* 2007;**27**:6229–6242.
63. Hirano M, Emmanuele V, Quinzii CM. Emerging therapies for mitochondrial diseases. *Essays Biochem* 2018;**62**:467–481.
64. Oost LJ, Kustermann M, Armani A, Blaauw B, Romanello V. Fibroblast growth factor 21 controls mitophagy and muscle mass. *J Cachexia Sarcopenia Muscle* 2019;**10**: 630–642.
65. Hamacher-Brady A, Brady NR, Gottlieb RA, Gustafsson AB. Autophagy as a protective response to Bnip3-mediated apoptotic signaling in the heart. *Autophagy* 2006;**2**: 307–309.
66. Chaanine AH, Gordon RE, Kohlbrenner E, Benard L, Jeong D, Hajjar RJ. Potential role of BNIP3 in cardiac remodeling, myocardial stiffness, and endoplasmic reticulum mitochondrial calcium homeostasis in diastolic and systolic heart failure. *Circ Heart Fail* 2013;**6**:572–583.
67. Chen Y, Liu Y, Dorn GW 2nd. Mitochondrial fusion is essential for organelle function and cardiac homeostasis. *Circ Res* 2011;**109**:1327–1331.
68. Papanicolaou KN, Kikuchi R, Ngoh GA, Coughlan KA, Dominguez I, Stanley WC, et al. Mitofusins 1 and 2 are essential for postnatal metabolic remodeling in heart. *Circ Res* 2012;**111**:1012–1026.
69. Ikeda Y, Shirakabe A, Maejima Y, Zhai P, Sciarretta S, Toli J, et al. Endogenous Drp1 mediates mitochondrial autophagy and protects the heart against energy stress. *Circ Res* 2015;**116**:264–278.
70. Wai T, Garcia-Prieto J, Baker MJ, Merkwirth C, Benit P, Rustin P, et al. Imbalanced OPA1 processing and mitochondrial fragmentation cause heart failure in mice. *Science* 2015;**350**:aad0116.
71. Lin L, Zhang M, Yan R, Shan H, Diao J, Wei J. Inhibition of Drp1 attenuates mitochondrial damage and myocardial injury in Coxsackievirus B3 induced myocarditis. *Biochem Biophys Res Commun* 2017;**484**: 550–556.
72. Wu B, Li J, Ni H, Zhuang X, Qi Z, Chen Q, et al. TLR4 activation promotes the progression of experimental autoimmune myocarditis to dilated cardiomyopathy by inducing mitochondrial dynamic imbalance. *Oxid Med Cell Longev* 2018;**2018**: 3181278.
73. Landes T, Emorine LJ, Courilleau D, Rojo M, Belenguer P, Arnauné-Pelloquin L. The BH3-only Bnip3 binds to the dynamin Opa1 to promote mitochondrial fragmentation and apoptosis by distinct mechanisms. *EMBO Rep* 2010;**11**:459–465.
74. Picard M, McManus MJ, Csordas G, Varnai P, Dorn GW 2nd, Williams D, et al. Trans-mitochondrial coordination of cristae at regulated membrane junctions. *Nat Commun* 2015;**6**:6259.
75. Jarosz J, Ghosh S, Delbridge LMD, Petzer A, Hickey AJR, Crampin EJ, et al. Changes in mitochondrial morphology and organization can enhance energy supply from mitochondrial oxidative phosphorylation in diabetic cardiomyopathy. *Am J Physiol Cell Physiol* 2017;**312**:C190–C197.
76. von Haehling S, Morley JE, Coats AJS, Anker SD. Ethical guidelines for publishing in the Journal of Cachexia, Sarcopenia and Muscle: update 2019. *J Cachexia Sarcopenia Muscle* 2019;**10**:1143–1145.